*J. Fluid Mech.* (2013), *vol.* 722, *pp.* 618–644. © Cambridge University Press 2013 
doi:10.1017/jfm.2013.90

# Stability and sensitivity analysis in a simplified solid rocket motor flow

**G. Boyer[1,†], G. Casalis[2] and J. L. Estivalèzes[2]**

[1]CNES - Direction des Lanceurs, 52 rue Jacques Hillairet, 75612 Paris CEDEX, France
[2]ONERA, The French Aerospace Lab, 2 avenue douard Belin, B.P. 74025, 31055 Toulouse CEDEX 4, France

(Received 11 May 2012; revised 1 February 2013; accepted 8 February 2013; first published online 28 March 2013)

The present article aims at enhancing the computation of the global stability modes of the internal flow of solid rocket motors (SRMs) approximated by the Taylor–Culick solution. This modal approach suffers from the consequences of the non-normality of the global linearized incompressible Navier–Stokes operator, namely the lack of robustness of the eigenvalues that can lead to the computation of pseudo-modes rather than actual eigenmodes. In this respect, the effects of non-normality associated with strongly amplified eigenfunctions are highlighted on a simplified convective–diffusive stability problem with uniformly accelerated base state, the latter property being a typical characteristic of the Taylor–Culick flow. Non-convergence zones for the eigenvalues are exhibited for large Reynolds numbers and are related to the critical sensitivity to disturbances applied to one of the boundary conditions. For this reason, and according to experimental and numerical data related to the stability of simplified SRMs, a global stability analysis is performed assuming that the hydrodynamic fluctuations emerge from a geometrical defect applied at the sidewall. This comes to fix the upstream boundary condition at the abscissa of the sidewall disturbance. The resulting eigenmodes are shown to be discrete, numerically converged, well identified by a finite number of points of undefined phase of the velocity fluctuations. They marginally depend on Reynolds number variations, but are modified by changes on the boundaries location. As in the simplified problem, the inflow boundary condition is the most critical in terms of sensitivity to numerical errors, although not dramatic. Finally, the sensitivity analysis to infinitesimal base flow changes indicates that the variations applied close to the inflow boundary condition induce the largest move of the eigenvalues. In spite of the large non-normal effects induced by the large polynomial growth of the eigenfunctions, this paper shows that discrete instabilities may emerge from a wall defect, in contrast to configurations without such a geometrical perturbation whose dynamics may be rather driven by pseudo-modes.

**Key words:** absolute/convective instability, control instability, vortex shedding

† Present address: Institut de Radioprotection et de Sûreté Nucléaire (IRSN), BP3, 13115 Saint Paul-lez-Durance, France. Email address for correspondence: germain.boyer@irsn.fr

https://doi.org/10.1017/jfm.2013.90 Published online by Cambridge University Press

## 1. Introduction

In the past decade, the stability analysis of the incompressible Navier–Stokes equations has played a major role in the comprehension of the internal pressure oscillations occurring in large segmented solid rocket motors (SRMs) such as those of the European Ariane 5 launcher and the American Titan IV. Indeed, these motors exhibit several pressure bursts whose discrete frequencies occur nearby those of the axial acoustics. Although these oscillations were primarily thought to result from acoustic instabilities, as assumed in the acoustic balance method introduced by Culick (1966) and enhanced by Flandro (1995) and Flandro & Majdalani (2003), Majdalani, Fischbach & Flandro (2006) and Majdalani (2009), several vortex-shedding phenomena, numerically described by Vuillot (1995), are now understood to be the triggering factor of pressure oscillations. In particular, several cold gas experiments have highlighted the existence of parietal vortical structures growing all along the motor close to the propellant surface modelled as a blowing wall (Yagodkin 1967; Brown *et al.* 1981; Dunlap *et al.* 1990; Avalon & Josset 2006). Amongst the various hydrodynamic phenomena triggering the pressure oscillations, the predominance of this so-called 'parietal vortex shedding' (PVS) has been shown by reduced-scale firings performed in simplified configurations (Prévost & Godon 2005).

In this respect, the PVS can be modelled as a hydrodynamic instability of the Taylor–Culick solution (Taylor 1956; Culick 1966) that is a widely used as a steady approximation of the internal flow of SRMs for theoretical purposes, even if compressible or viscous disturbances are sought (Varapaev & Yagodkin 1969; Flandro & Majdalani 2003; Majdalani 2009). The local approach first introduced by Varapaev & Yagodkin (1969), further used by Casalis, Avalon & Pineau (1998) and enhanced by Griffond & Casalis (2001) consisted of computing the local incompressible, viscous disturbances of the Taylor–Culick flow. It did show the existence of convectively amplified modes whose shape is similar to the experimental PVS in the laminar zone of the motor. Then, global stability modes were tentatively pursued by Chedevergne, Casalis & Feraille (2006) according to the general works of Theofilis (2003), so as to explain the frequency selection of the experimentally observed pressure oscillations. A branch of temporally stable modes resulting from the imposed conditions at the front wall and the downstream boundary of the computational domain showed very good agreement with the pressure bursts experimentally observed in cold gas set-ups and occurring at constant values of $fR/V_{inj}$, where $f$ is the actual burst frequency, $R$ the average radius of the motor internal fluid section and $V_{inj}$ the parietal fluid velocity injection. The spatial features of the related eigenfunctions, namely the axial amplification and the radial profile of the velocity fluctuations, were consistent with experimental data (Chedevergne *et al.* 2006) and results derived from the local approach. However, the physical relevance of these eigenmodes, evidenced by the numerical simulations of Chedevergne, Casalis & Majdalani (2012), is marred by their large dependence on the employed axial discretization (Chedevergne 2007). Conversely, according to several simplified reduced-scale firings (Prévost & Godon 2005), the emergence of pressure oscillations and PVS structures with large amplitude and well-separated frequencies is largely eased by the existence of small geometrical disturbances such as intersegments or even wall defects. From this standpoint, a perturbation including a modelled geometrical disturbance has been taken into account in the global stability analysis of SRMs by Boyer, Casalis & Estivalèzes (2012). More precisely, numerical simulations have shown that the hydrodynamic structures related to the PVS emerge from such a disturbance. A global stability analysis of the Taylor–Culick flow has then been performed on the domain comprised

https://doi.org/10.1017/jfm.2013.90 Published online by Cambridge University Press

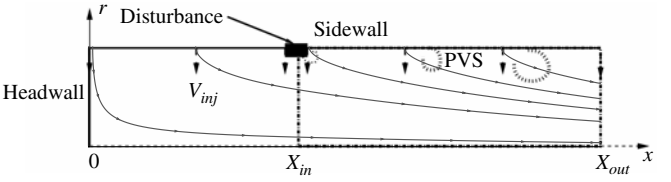



FIGURE 1. Schematic view of the global stability analysis performed when a geometrical disturbance is applied to the blowing wall. Here $V_{inj}$ designates the wall injection velocity, $X_{in}$ the reduced abscissa of the wall defect and $X_{out}$ the duct aspect ratio, the duct radius $R$ being the reference length. The PVS structures (dotted lines) are shown to emerge from the wall disturbance (Boyer *et al.* 2012). The dash-dotted lines enclose the resulting stability analysis domain. The grey lines depict the stream lines of the Taylor–Culick flow.

between the axial location of the wall defect and the duct outflow (figure 1). The resulting eigenmodes were discrete, showed an effective convergence regarding the used discretization and the related eigenfunctions were in good agreement with the simulated vortical structures.

From a theoretical point of view, the encountered difficulties in the numerical resolution of this stability problem may come from a characteristic feature of the linearized Navier–Stokes equations, namely the effects of non-normality. According to the work of Trefethen *et al.* (1993), the eigenvalues related to non-normal operators can easily be destabilized by small perturbations applied to physical parameters or by small numerical disturbances. In the same way, large sets of approximate solutions up to an arbitrary accuracy, called pseudo-modes, can be exhibited in such cases. That is why, for robustness reasons, the optimal framework, introduced for instance by Sipp and co-workers (Monokrousous *et al.* 2010; Sipp, Marquet & Meglia 2010; Brandt *et al.* 2011), might better suit to the study of hydrodynamic instabilities occurring for instance in boundary layers and separate flows than the modal approach widely used so far (Ehrenstein & Gallaire 2005; Alizard & Robinet 2007; Åkervik *et al.* 2008). In the present case, the non-normality effects may be all the more critical as the resulting eigenfunctions are much more spatially amplified than those occurring in boundary layers because of the base flow axial amplification. They may therefore explain not only the large sensitivity of the eigenmodes, but also the previously observed strong mesh dependence itself.

The present paper aims at showing that the modal stability analysis of the Taylor–Culick flow leads to discrete, converged hydrodynamic modes that can be tentatively used to model the experimentally observed PVS instabilities. First, referring to the simplified stability modelling introduced by Trefethen & Embree (2005), the non-normality effects will be evaluated on a mono-dimensional convective–diffusive eigenvalue problem whose convective term is proportional to the axial coordinate as for the Taylor–Culick flow. Such a study allows us to better understand the numerical issues encountered in the computation of the global modes and justify the ansatz introduced by Boyer *et al.* (2012). As a consequence, the global hydrodynamic instabilities of the Taylor–Culick flow that are assumed to propagate from a wall defect down to the duct exit will be further depicted. Their negligible dependence on the used mesh and their discreteness has to be confirmed, and the influence of the non-dimensional parameters of the problem, namely the Reynolds number ($Re$) and the location of the axial boundaries ($X_{in}$ for the injection break and $X_{out}$ for the outflow) will be investigated. A sensitivity analysis, based on the computation

https://doi.org/10.1017/jfm.2013.90 Published online by Cambridge University Press

of both direct and adjoint eigenfunctions as described by Hill (1995), will also be carried out. On the one hand, it will be used to assess the numerical sensitivity of the computed eigenmodes and confirm their relevance. On the other hand, according to the framework used by Bottaro, Corbett & Lucchini (2003) and Tumin (2003) in boundary layer stability and by Marquet, Sipp & Jacqin (2008) for the cylinder flow, the effect of base flow distortions on these eigenmodes will be computed and the areas of largest sensitivity will be described.

The paper proceeds hereafter as follows. First (§ 2), a simplified convective–diffusive operator with uniformly accelerated convection velocity is studied: approximate eigenmodes and $\varepsilon$-pseudo-spectra subsets are analytically calculated, and then compared with numerical integration results. The sensitivity to disturbances is also presented so as to illustrate the effects of non-normality. Then (§ 3), the global stability of the Taylor–Culick flow is performed on a subdomain whose upstream boundary coincides with a spatial disturbance from which potential instabilities emerge. The influence of the Reynolds number and the location of the domain boundaries is then investigated. Finally (§ 4), the boundary conditions and base flow sensitivities of the global eigenvalues are calculated to evaluate the robustness of the previous eigenmodes.

## 2. A convective–diffusive simplified case

This section aims at more precisely describing the numerical problems occurring in the computation the eigenmodes of the incompressible Navier–Stokes equations linearized around the Taylor–Culick solution. As shown by Trefethen & Embree (2005) on a simplified convective–diffusive problem and Sipp *et al.* (2010) in global stability analyses, these problems are basically due to the non-normality of the stability operators which induce non-orthogonal eigenfunctions, large transient effects associated with a sum of eigenmodes, and a large sensitivity of the eigenmodes to numerical errors. In the present work, these issues are expected to be even more critical than in the computation of the global convective instabilities occurring for instance in boundary layers. Indeed, the hydrodynamic instabilities sought in SRMs have been shown to grow polynomially with the axial coordinate (Griffond & Casalis 2001). Correlatively, Chedevergne (2007) has shown that the eigenvalues resulting from a global stability of these motors do not reach a fixed location in the complex plane when the axial discretization is arbitrarily refined, even if their related eigenfunctions show a very good agreement with the local ones and the vortical structures measured in cold gas set-ups (Chedevergne *et al.* 2006). These features might be related to a fundamental difference between the boundary layer stability problems and the present one, i.e. the strong non-parallelism of the Taylor–Culick flow used as a base state here.

That is why, following Trefethen's approach, a simplified axial convective–diffusive stability problem with uniformly accelerated convection of the fluctuations is introduced in this section. The analytical integration of this modelling aims at highlighting the specific numerical issues due to the combined effects of the non-normality of the linearized Navier–Stokes equations and the huge non-parallelism of base states such as the Taylor–Culick flow. This problem, defined for $x \in [0, 1]$, reads

$$\mathscr{A}\hat{u} - \mathrm{i}\hat{\omega}\hat{u} = 0 \quad \text{with } \mathscr{A}\hat{u} = -\frac{1}{Re}\hat{u}'' + x\hat{u}' \tag{2.1}$$

https://doi.org/10.1017/jfm.2013.90 Published online by Cambridge University Press

with the homogeneous boundary conditions $\hat{u}(0) = 0$ and $\hat{u}'(1) = 0$. Here the prime $'$ stands for the derivative with respect to $x$. In expression (2.1), $Re$ denotes a Reynolds number by analogy with the viscous term of the linearized incompressible Navier–Stokes equations. The first derivative term $x\hat{u}'$ represents the convection of the eigenfunctions by a uniformly accelerated velocity as in the stability problem occurring in solid propellant rocket motors. In the same way, boundary conditions are called 'inlet' ($x = 0$) and 'outlet' ($x = 1$) conditions since they are analogous to the boundary conditions which will be used in the global stability problem in § 3. Note that this problem might have been defined for $x \in [0, X_{out}]$ with $X_{out} > 0$. The current definition would have been recovered by changing $x$ into $x/X_{out}$ and $Re$ into $ReX_{out}^2$.

### 2.1. *Matched asymptotic developments*

An approximate solution of the stability problem (2.1) is sought for as a matched asymptotic expansion for large Reynolds numbers. Since the Reynolds number is assumed to be large, the viscous effects are expected to be negligible on a large part $[0, a]$, $a > 0$, of the domain and the eigenfunctions $\hat{u}$ to be similar to the solutions $u(x) = x^{i\omega}$, $\mathrm{Im}(\omega) < 0$ of the non-viscous problem $\{xu' - i\omega u = 0; u(0) = 0\}$. Therefore $\hat{u}$ can be approximated by the $N$th-order expansion $\hat{u}(x) \approx U_N(x) = u_0(x) + Re^{-1}u_1(x) + \cdots + Re^{-N}u_N(x)$ with respect to the small parameter $Re^{-1}$. As shown in § A.1, a set of $N$ approximate eigenvalues denoted as $\Lambda_N(\mathscr{A}) = \{-(2m+1)i, m = 0 \ldots N\}$ is obtained together with the $N$ following eigenfunctions

$$\left\{ U_m(x) = \sum_{n=0}^{m} \frac{(2m+1)!\; x^{2(m-n)+1}}{(2(m-n)+1)!\; n!\; (-2Re)^n} \right\}_{m=0,\ldots,N} \tag{2.2}$$

that exactly verify (2.1) and $\hat{u}_m(0) = 0$. The above eigenvalues are all located on the negative part of the imaginary axis, and the related eigenfunctions are growing polynomially with $x$. They are called 'external solutions' by analogy with the external part of a boundary layer where the viscous effects are neglected. In contrast, this external solution must be modified at $x = 1$ to match with the second boundary condition. Therefore, an 'internal solution' is calculated thanks to the variable change $\hat{v}(X = Re(1-x)) = \hat{u}(x)$ which aims at precisely modelling the sharp variations of the eigenfunctions close to $x = 1$. Once again $\hat{v}$ is expanded up to a given order $K$ as $\hat{v}(X) \approx U_K(X) = v_0(X) + Re^{-1}v_1(X) + \cdots + Re^{-K}v_K(X)$.

As detailed in § A.2, $V_K$ is separated into two terms denoted as $V_{K,1}$ and $V_{K,2}$. $V_{K,1}$ is a polynomial function of $X$ and $Re$ and is identified to the $m$th internal eigenfunction $U_m$ if $K = 2m + 1$, and therefore verifies (2.1) and the inflow boundary condition. Here $V_{K,2}$, which exactly satisfies (2.1) and the outflow boundary condition, can be expressed as

$$\hat{v}_{K,2}(X) = \left( \sum_{k=0}^{K} Q_k(X) \right) \mathrm{e}^{-X} \tag{2.3}$$

where each $Q_k$ denotes a set of polynomial functions of degree $2k - 2$. Since the above asymptotic expansions are valid regardless of the order $N$ of the external solution that is chosen, a complete set of approximate eigenvalues $\Lambda(\mathscr{A}) = \{-(2m+1)i, m \in \mathbb{N}\}$ related to the polynomially growing eigenfunctions

$$\left\{ \hat{u}_m(x) = \sum_{n=0}^{m} \frac{(2n+1)!\; x^{2(m-n)+1}}{n!\; (-2Re)^n} + \left( \sum_{k=0}^{2m+1} Q_k(Re(1-x)) \right) \mathrm{e}^{Re(x-1)} \right\}_{m \in \mathbb{N}} \tag{2.4}$$

https://doi.org/10.1017/jfm.2013.90 Published online by Cambridge University Press

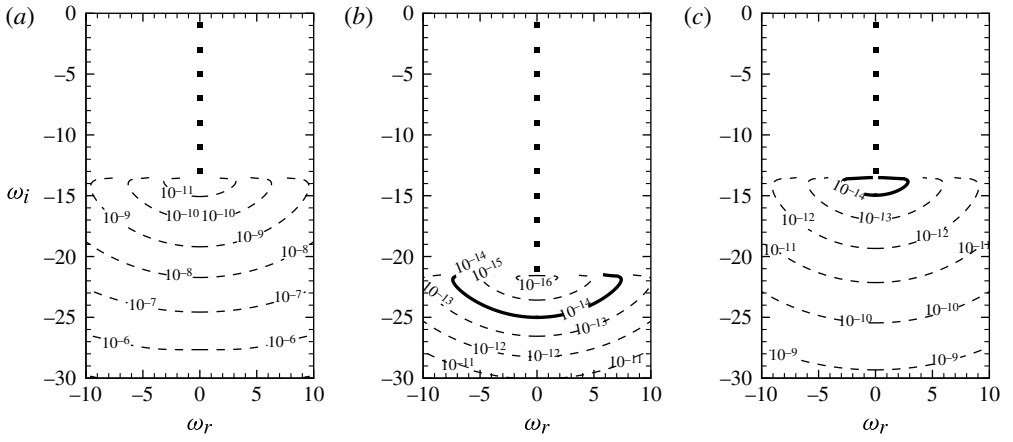



FIGURE 2. Eigenvalues of the $N$th-order approximation of the direct eigenvalue problem (■) and level lines of its resolvent norm (- - -) for various Reynolds numbers: (*a*) $Re = 200$, $N = 6$; (*b*) $Re = 200$, $N = 10$; (*c*) $Re = 500$, $N = 6$. The particular line (—) defines the zone where the resolvent norm is lower than the numerical accuracy $\varepsilon_M \approx 10^{-14}$ and where no eigenvalue can be computed.

is then obtained. These solutions exhibit a polynomial growth along $x$ and are ended by a boundary layer whose characteristic size, driven by the term $e^{Re(x-1)}$, is proportional to the inverse of the Reynolds number.

Now, the robustness of these eigenmodes can be further investigated. For this purpose, let us consider the external asymptotic expansion $U_N$ calculated for a fixed order $N$ and $\omega \notin \Lambda_N(\mathscr{A})$. Note that $U_N$ verifies the inflow boundary condition, and if $-\mathrm{Im}(\omega) > 2N + 3/2$, then the norm of the residual function $r_N(\hat{\omega}) = (\mathscr{A} - \mathrm{i}\hat{\omega})U_N$ expressed in (A 4) can be evaluated. In particular, one obtains

$$\frac{\|r_N(\hat{\omega})\|}{\|U_N\|} = \frac{2c_{N+2}(\hat{\omega})}{(2Re)^{N+1}N!\|U_N\|}\int_0^1 x^{-2\mathrm{Re}(\hat{\omega})-4N-4}\mathrm{d}x. \tag{2.5}$$

Therefore, for a given $\varepsilon$, the subset

$$\Lambda'_{\varepsilon,N}(\mathscr{A}) = \left\{\hat{\omega}\in\mathbb{C} \Big/ \frac{\|r_N(\hat{\omega})\|}{\|U_N\|} \leqslant \varepsilon, \mathrm{Im}(\hat{\omega}) < -(2N+3/2)\right\} \tag{2.6}$$

of the $\varepsilon$-pseudo-spectrum $\Lambda_\varepsilon(\mathscr{A})$ defined as

$$\Lambda_\varepsilon(\mathscr{A}) = \left\{\omega\in\mathbb{C} \text{ such as } \frac{\|(\mathscr{A}-\mathrm{i}\omega)u\|}{\|u\|} \leqslant \varepsilon \text{ for some } u\right\} \tag{2.7}$$

can be calculated. If the order $N$ of the asymptotic expansion is large enough, this subset $\Lambda'_{\varepsilon,N}(\mathscr{A})$ is not empty, which means that a continuous set of pseudo-eigenmodes up to a precision of $\varepsilon$ can be exhibited. In figure 2, the contour lines of $\Lambda'_{\varepsilon,N}(\mathscr{A})$ are plotted for various Reynolds numbers $Re$, the order of the asymptotic expansion $N$ and values of $\varepsilon$. Let us consider in particular the subsets calculated for $\varepsilon = 10^{-14}$, $Re = 200$ and $N = 10$ or $Re = 500$ and $N = 6$. If an eigenvalue is numerically sought in these areas, it can hardly be computed correctly because pseudo-eigenpairs satisfying the problem equations with the same numerical accuracy may be exhibited in its very vicinity. In this respect, a sensitivity analysis of the eigenmodes

https://doi.org/10.1017/jfm.2013.90 Published online by Cambridge University Press

that are close to the limit of numerical accuracy may be useful to determine the terms of the eigenvalue problem (2.1) associated with its homogeneous boundary conditions that most easily destabilize the eigenmodes computation.

### 2.2. *Sensitivity to numerical disturbances on the boundary conditions*

Referring to the sensitivity formalism introduced for instance by Airiau (2000) and Bottaro *et al.* (2003), the adjoint equations associated with the direct problem (2.1) can be used to evaluate the effect of numerical disturbances on the eigenvalues. Considering the usual dot product $\langle\ ,\ \rangle$ on $\mathscr{L}^2([0,1])$, the adjoint eigenvalue problem $(\mathscr{A}^\dagger - \mathrm{i}\tilde{\omega})\tilde{u} = 0$ is defined by the relation

$$\forall \hat{u}, \tilde{u}, \quad \langle \tilde{u}, (\mathscr{A} - \mathrm{i}\hat{\omega})\hat{u}\rangle = \langle (\mathscr{A}^\dagger - \mathrm{i}\tilde{\omega})\tilde{u}, \hat{u}\rangle \tag{2.8}$$

where $\tilde{u}$ and $\tilde{\omega}$ denote the adjoint eigenvalue and eigenfunction. Referring to the method devised by Hill (1995) for the boundary layer receptivity, the left-hand side of (2.8) can also be derived to obtain the following Lagrange identity

$$\begin{aligned}\langle \tilde{u}, (\mathscr{A}\hat{u} - \mathrm{i}\hat{\omega})\hat{u}\rangle - \langle (\mathscr{A}^\dagger - \mathrm{i}\tilde{\omega})\tilde{u}), \hat{u}\rangle = \frac{1}{Re}([\hat{u}\tilde{u}'^*]_0^1 - [\hat{u}'\tilde{u}^*]_0^1) \\ + [\hat{u}\tilde{u}^*]_0^1 + \mathrm{i}(\tilde{\omega}^* + \hat{\omega})\langle \tilde{u}, \hat{u}\rangle\end{aligned} \tag{2.9}$$

which leads to the adjoint operator $\mathscr{A}^\dagger$ defined as

$$\mathscr{A}^\dagger \tilde{u} = -\frac{1}{Re}\tilde{u}'' - x\tilde{u}' - \tilde{u} \tag{2.10}$$

and associated with the homogeneous boundary conditions $\tilde{u}(0) = 0$ and $Re^{-1}\tilde{u}'(1) + \tilde{u}(1) = 0$ provided that $\tilde{\omega} = -\hat{\omega}^*$. Note that if $\hat{\omega}$ and $\tilde{\omega}$ are a couple of direct and adjoint eigenvalues such that $\tilde{\omega} \neq -\hat{\omega}^*$ related to eigenfunctions $\hat{u}_{\hat{\omega}}$ and $\tilde{u}_{\tilde{\omega}}$, then $\langle \tilde{u}_{\tilde{\omega}}, \hat{u}_{\hat{\omega}}\rangle = 0$. As a consequence, the direct and adjoint eigenvectors form a biorthogonal set of $\mathscr{L}^2(\Omega)$.

The relation (2.9) is then used to estimate the influence of small disturbances of amplitude $\varepsilon \ll 1$ applied to the inflow and outflow boundary conditions that are written as $\hat{u}(0) + \varepsilon\delta\hat{u}(0) = \varepsilon u_0$ and $\hat{u}'(1) + \varepsilon\delta\hat{u}'(1) = \varepsilon u_1$. Consequently, the eigensolutions of the direct problem are sought for as a sum of a non-disturbed part and a disturbance of amplitude $\varepsilon$, i.e. $(\hat{\omega} + \varepsilon\delta\hat{\omega}, \hat{u} + \varepsilon\delta\hat{u})$. Linearizing relation (2.9) yields

$$\delta\hat{\omega} = \mathrm{i}\left(\frac{(\delta\hat{u}(0)\tilde{u}'^*(0) - \delta\hat{u}'(1)\tilde{u}^*(1))}{Re\langle \tilde{u}, \hat{u}\rangle}\right). \tag{2.11}$$

This relation can be formally rewritten as $\delta\hat{\omega} = \sum(\nabla_{f_i}, \delta f_i)$ where the $\nabla_{f_i}$ are the sensitivity functions with respect to the parameters $f_i$. More precisely, the sensitivity functions read

$$\nabla_{\hat{u}(0)}(x) = -\mathrm{i}Re^{-1}\tilde{u}'^*(0)\delta_D(x)/\langle \tilde{u}, \hat{u}\rangle, \tag{2.12}$$

$$\nabla_{\hat{u}'(1)}(x) = -\mathrm{i}Re^{-1}\tilde{u}^*(1)\delta_D(x-1)/\langle \tilde{u}, \hat{u}\rangle. \tag{2.13}$$

where $\delta_D$ is the Dirac function.

Since the values of the adjoint eigenfunctions or their derivative at the boundaries explicitly arise in the above relations, the adjoint problem must be solved to evaluate these sensitivity functions. The direct and adjoint problems are therefore integrated numerically using a spectral collocation technique and the generalized eigenvalue solver implemented in the MATLAB function `eig`. Examples of direct and adjoint

https://doi.org/10.1017/jfm.2013.90 Published online by Cambridge University Press

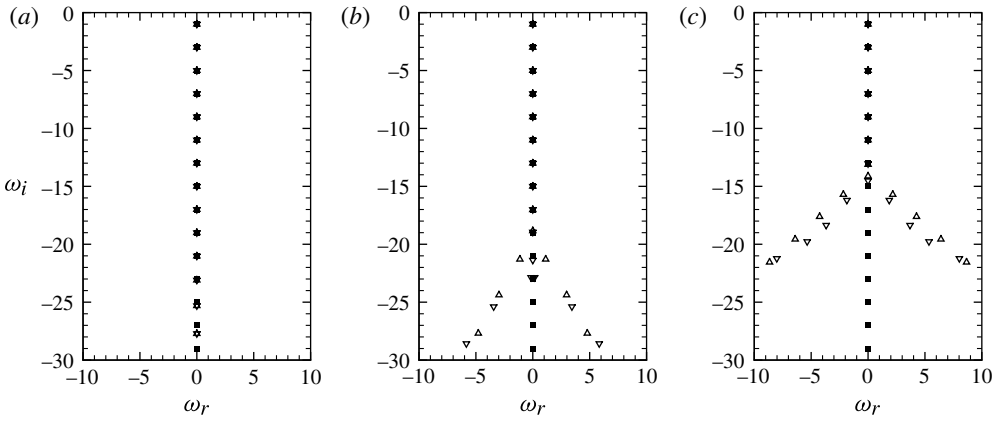



FIGURE 3. Comparison between the theoretical eigenvalues of the direct problem and the computed direct and adjoint eigenvalues, for various Reynolds numbers: (*a*) $Re = 100$; (*b*) $Re = 200$; (*c*) $Re = 500$. The symbols represent: ■, analytical solution; △, computed direct eigenvalues; ▽, computed adjoint eigenvalues, discretization by the spectral collocation method, $N = 200$ points.

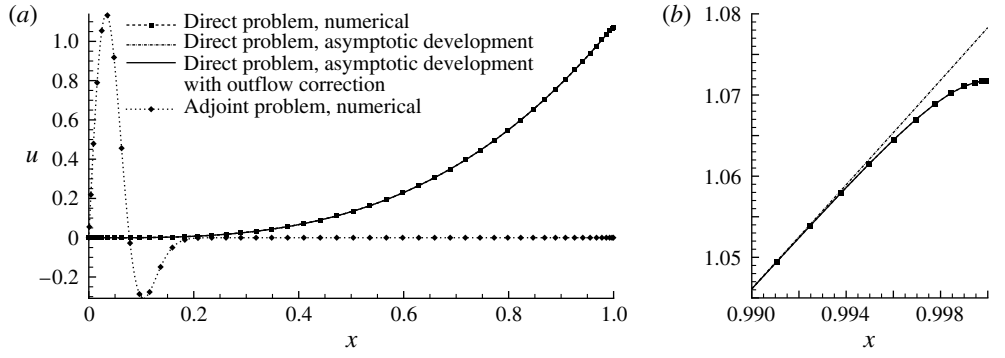



FIGURE 4. Direct and adjoint eigenfunctions related to the mode $\hat{\omega} = -3\mathrm{i}$ computed for $Re = 500$: (*a*) full view; (*b*) zoom close to $x = 1$. The direct eigenfunctions are normalized by $\hat{u}(0.97)$ and the adjoint ones are normalized by $\hat{u}(0.03)$. The approximate direct eigenfunctions, given in (2.4), are plotted as a comparison.

spectra are plotted in figure 3 for $Re = 100$, $Re = 200$ and $Re = 500$, as well as the related eigenfunctions computed for $Re = 500$ (figure 4); $N = 200$ collocation points are used. Interestingly, the direct and adjoint eigenvalues predicted by the analytic solution (2.4) are perfectly recovered down to a limit value of $\mathrm{Im}(\omega)$. Then, for $Re = 200$ and $Re = 500$, two symmetric branches are obtained instead of the theoretical pure imaginary eigenvalues. These branches exactly appear in the area of $\varepsilon$-pseudo-modes calculated for $\varepsilon = 10^{-14}$ as presented in figure 2. Note also that the theoretical shape of the direct eigenfunctions also matches with the computed ones; in particular, both polynomial downstream growth and outflow boundary layer are recovered exactly. In contrast, the adjoint eigenfunctions are even more amplified in the upstream direction than the direct ones are amplified in the downstream direction.

https://doi.org/10.1017/jfm.2013.90 Published online by Cambridge University Press

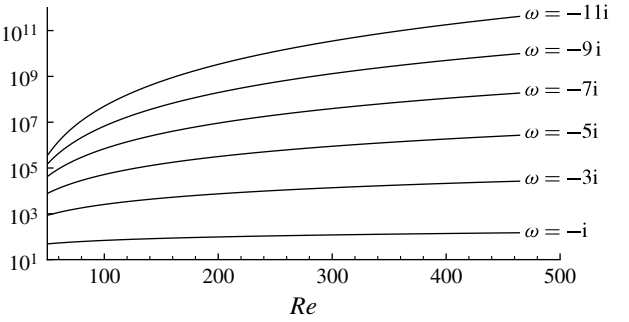



FIGURE 5. Evolution of the sensitivity function $\nabla_{\hat{u}(0)}$ related to a disturbance on the boundary condition at $x = 0$ for a varying Reynolds number. The first five eigenmodes modes are considered. The $y$-axis scale is logarithmic.

The direct and adjoint eigenfunctions reach their maximum amplitude in opposite zones of the domain. This is a characteristic feature of the so-called 'convective non-normality' as defined by Sipp *et al.* (2010). The non-normality can be quantified by the ratio $\zeta = \|\tilde{u}\|\|\hat{u}\|/\langle\tilde{u}, \hat{u}\rangle$ expressed for a couple of direct and adjoint eigenfunctions $\hat{u}$ and $\tilde{u}$ related to a same eigenmode. The closer to one, the less non-normal the operator; in contrast, $\zeta$ is much larger here because the direct and adjoint eigenfunctions are strongly amplified in opposite directions. As a consequence, the sensitivity functions (2.12), that are proportional to $1/\langle\tilde{u}, \hat{u}\rangle$, are naturally larger for highly non-normal operators. In practice, the sensitivity function of the outflow boundary condition is proportional to $\tilde{u}^*(1)$ that is exponentially small because of the upstream growth of the adjoint eigenfunctions. Numerically, $\delta\hat{\omega}$ has been computed in this case and is of the order of the machine accuracy as soon as $Re = 50$. This is consistent with the property that the approximate analytical solutions actually do no depend on this outflow condition. In contrast, the effects of the non-normality fully arise at the inflow boundary condition, because the dot product $\langle\tilde{u}, \hat{u}\rangle$ is small and the variations of the adjoint eigenfunctions close to $x = 0$ are very large, which makes the values reached by $\hat{u}'(0)$ even larger. As depicted in figure 5, this sensitivity increases with the Reynolds number and the order of the considered eigenmode. In particular, for a given disturbance of magnitude, say, $\varepsilon = 10^{-10}$, the eigenvalue related to the mode $\hat{\omega} = -9\mathrm{i}$ can undergo an amplitude shift $\varepsilon\delta\hat{\omega} = 1$ at $Re = 500$.

### 2.3. *Discussion*

The study of this convective–diffusive eigenvalue problem reveals two numerical issues that may occur in the integration of the linearized incompressible Navier–Stokes equations. First, the direct eigenfunctions, that are amplified downstream, exhibit a boundary layer at the outflow condition whose size decreases with the Reynolds number. Second, the analytical integration of this problem shows the existence of continuous sets of pseudo-eigenmodes that verify the stability problem up to an arbitrary precision $\varepsilon$. The existence of these pseudo-modes is due to the large sensitivity to small disturbances applied on the inflow boundary condition that can shift exact eigenvalues from their theoretical location. Wider areas of pseudo-eigenmodes for small $\varepsilon$ and more critical sensitivities are obtained when the Reynolds number is larger and the spatial growth of the eigenfunctions increase, or the related imaginary part of the eigenvalues or pseudo-eigenvalues is more negative. As in

https://doi.org/10.1017/jfm.2013.90 Published online by Cambridge University Press

Trefethen's convective–diffusive simplified modelling, the effects of the convective non-normality, in particular the opposite growths of the direct and adjoint eigenfunctions, together with the strength of these growths itself, are clearly identified in the formulation of the sensitivity functions and are understood to play a major role in the existence of such pseudo-eigenmodes and in the numerical non-convergence of the eigenvalues. The only difference with Trefethen's problem is the behaviour of the eigenvalues that become stabilized in the present case instead of closing up when the Reynolds number increase, and that do not depend on the outflow boundary condition.

All of these features related to non-normality are all the more likely to occur in the global stability of the Taylor–Culick flow as the latter is also uniformly accelerated and its instabilities are known to be polynomially amplified in the axial direction. In addition, the non-convergence of the eigenvalues when the axial discretization is increased has clearly been evidenced by Chedevergne (2007). Since these modes are correctly recovered in the numerical simulations carried out by Chedevergne *et al.* (2012), they must actually be pseudo-modes or they may belong to a continuous set of eigenmodes that is discretized because of the employed numerical method. In contrast, the modes computed on an axial subdomain $x \in [X_{in}, X_{out}]$, assuming that the related vortical structures emerge from a wall injection break imposed at $X_{in}$ seem to be actual discrete modes, as stated by Boyer *et al.* (2012). Indeed, according to the above results, the sensitivity of the inflow condition may be less critical in this latter case because the singularity induced by the base flow at $x = 0$ is avoided. Therefore, in the following sections, these modes are more precisely described and their numerical sensitivity is evaluated.

## 3. Global stability of a simplified SRM

### 3.1. *Direct and adjoint problems*

In this section, the hydrodynamic instabilities that occur in a simplified SRM with cold-gas normal wall injection are investigated. We consider a cylindrical duct of unitary radius $R = 1$ and length-to-radius aspect ratio $X_{out}$. The non-dimensional axial and radial coordinates are denoted as $x$ and $r$; the flow is supposed to be axisymmetric, so that the azimuthal coordinate $\theta$ will not be used. The fluid domain is a part of this duct delimited by the inflow and outflow reduced abscissae $X_{in}$ and $X_{out}$, so that $(x, r)$ belong to $[X_{in}, X_{out}] \times [0, 1]$, as depicted in figure 1. The parietal fluid injection induces a constant and uniform wall velocity $V_{inj}$ that is the reference velocity used for non-dimensionalization. The reference pressure, density and kinetic viscosity $p_0$, $\rho_0$ and $\mu_0$ are those evaluated at the head end $x = 0$. In this respect, the parietal Reynolds number $Re = \rho_0 V_{inj} R/\mu_0$ is introduced to characterize the viscosity effects. Let also $\boldsymbol{U} = (U_x, U_r)$ be the laminar Taylor–Culick steady base velocity that usually approximates the internal SRM flows, and that reads

$$U_x(x, r) = \pi x \cos\left(\frac{\pi r^2}{2}\right) \quad \text{and} \quad U_r(x, r) = -\frac{1}{r}\sin\left(\frac{\pi r^2}{2}\right). \tag{3.1}$$

Note that, as in the previous simplified case, the average flow is uniformly accelerated. The small unsteady perturbations $(p', \boldsymbol{u}')$ to this base state are sought for as $(p', \boldsymbol{u}') = (\hat{p}, \hat{\boldsymbol{u}})\mathrm{e}^{-\mathrm{i}\hat{\omega}t}$, with $\hat{\boldsymbol{u}} = (\hat{u}_x, \hat{u}_r)$ for axisymmetric disturbances and $\hat{\omega}$ the complex circular frequency of the normal-mode disturbances. Note that an azimuthal dependence of the pressure and velocity field, as well as the existence of an azimuthal velocity component, are deliberately not taken into consideration. Indeed, previous works carried out by Griffond & Casalis (2001) in the local stability framework

https://doi.org/10.1017/jfm.2013.90 Published online by Cambridge University Press

show that, amongst the PVS modes sought as $q'(x, r, \theta, t) = \hat{q}(r)\mathrm{e}^{\mathrm{i}(kx+m\theta-\omega t)}$, the spatial modes obtained for $m = 0$ are the most amplified for a given $\omega$. Therefore, only axisymmetric modes are sought in this study. In these conditions, the non-dimensional linearized incompressible Navier–Stokes equations are written as

$$\mathscr{A}(\hat{p}, \hat{\boldsymbol{u}}) = \mathrm{i}\hat{\omega}\mathscr{B}(\hat{p}, \hat{\boldsymbol{u}}), \tag{3.2}$$

where $\mathscr{A}$ and $\mathscr{B}$ are the operators

$$\mathscr{A}(\hat{p}, \hat{\boldsymbol{u}}) = \begin{pmatrix} \boldsymbol{\nabla}\cdot\hat{\boldsymbol{u}} \\ -\dfrac{1}{Re}\Delta\hat{\boldsymbol{u}} + (\boldsymbol{U}\cdot\boldsymbol{\nabla})\hat{\boldsymbol{u}} + (\hat{\boldsymbol{u}}\cdot\boldsymbol{\nabla})\boldsymbol{U} + \boldsymbol{\nabla}\hat{p} \end{pmatrix} \quad \text{and} \quad \mathscr{B}(\hat{p}, \hat{\boldsymbol{u}}) = \begin{pmatrix} 0 \\ \hat{\boldsymbol{u}} \end{pmatrix}. \tag{3.3}$$

The boundary conditions shall ensure that the weak form of the above system is well posed: the velocity fluctuations are set equal to zero at the inlet and the wall, the normal stress tensor is set equal to zero at the outflow, and simple symmetry conditions are imposed on the axis. One obtains

$$\partial_r\hat{p}(x, 0) = \partial_r\hat{u}_x(x, 0) = \hat{u}_r(x, 0) = 0 \quad \forall x \in [X_{in}, X_{out}] \tag{3.4a}$$

$$\hat{\boldsymbol{u}}(X_{in}, r) = 0 \quad \forall r \in [0, 1] \tag{3.4b}$$

$$\hat{\boldsymbol{u}}(x, 1) = 0 \quad \forall x \in [X_{in}, X_{out}] \tag{3.4c}$$

$$\boldsymbol{\sigma}(\hat{p}, \hat{\boldsymbol{u}})\cdot\boldsymbol{e}_x(X_{out}, r) = 0 \quad \forall r \in [0, 1] \tag{3.4d}$$

where $\boldsymbol{e}_x$ is the unitary normal vector in the axial direction and $\boldsymbol{\sigma}$ the stress tensor defined by

$$\boldsymbol{\sigma}(\hat{p}, \hat{\boldsymbol{u}}) = -\frac{1}{Re}(\boldsymbol{\nabla}\hat{\boldsymbol{u}} + \alpha_{out}\boldsymbol{\nabla}\hat{\boldsymbol{u}}^{\mathrm{T}}) + \beta_{out}\hat{\boldsymbol{u}}\cdot\boldsymbol{U}^{\mathrm{T}} + \hat{p}\boldsymbol{\delta}. \tag{3.5}$$

The normal component is set equal to zero at the outflow. In the above expression, superscript T denotes transpose, and $\alpha_{out}$ and $\beta_{out}$ are additional parameters. If $\alpha_{out} = 1$ and $\beta_{out} = 0$, the classic expression of the stress tensor is recovered. Otherwise, these parameters can be chosen as follows without altering the problem wellposedness: $\alpha_{out}$ can be set equal to zero since the fluid is incompressible, and $\beta_{out}$ can be chosen between 0 and $1/2$.

Once again, the relation between the direct and adjoint problems is given by the Lagrange identity. Let $\langle , \rangle$ denote the Hermitian dot product on $(\mathscr{L}^2(\Omega))^3$, $[\boldsymbol{g}]_\Gamma = \int_\Gamma \boldsymbol{g}\cdot\boldsymbol{n}\,\mathrm{d}\sigma$ the integral on the domain boundary of a function, vector or tensor $\boldsymbol{g}$, and superscript $H$ the tensors trans-conjugate. Then the Green's theorem yields

$$\begin{aligned} &\langle\tilde{p}, \tilde{\boldsymbol{u}}; (\mathscr{A} - \mathrm{i}\hat{\omega}\mathscr{B})(\hat{p}, \hat{\boldsymbol{u}})\rangle - \langle(\mathscr{A}^\dagger - \mathrm{i}\tilde{\omega}\mathscr{B}^\dagger)(\tilde{p}, \tilde{\boldsymbol{u}}); \hat{p}, \hat{\boldsymbol{u}}\rangle \\ &\quad = \mathrm{i}(\tilde{\omega}^* - \hat{\omega})\langle\tilde{\boldsymbol{u}}^H\cdot\hat{\boldsymbol{u}}\rangle + [\tilde{\boldsymbol{u}}\cdot\boldsymbol{\sigma}(\hat{p}, \hat{\boldsymbol{u}}) - \boldsymbol{\sigma}^{\dagger H}(\tilde{p}, \tilde{\boldsymbol{u}})\cdot\hat{\boldsymbol{u}}]_\Gamma \end{aligned} \tag{3.6}$$

where $(\tilde{p}; \tilde{\boldsymbol{u}})$ are the adjoint pressure and velocity fluctuations, $\tilde{\omega}$ the adjoint complex circular frequency, $\mathscr{A}^\dagger$ and $\mathscr{B}^\dagger = \mathscr{B}$ the adjoint spatial and temporal operators defined on the domain $\Omega$ by

$$\mathscr{A}^\dagger(\tilde{p}, \tilde{\boldsymbol{u}}) = \begin{pmatrix} -\boldsymbol{\nabla}\cdot\tilde{\boldsymbol{u}} \\ -\dfrac{1}{Re}\Delta\tilde{\boldsymbol{u}} - (\boldsymbol{U}\cdot\boldsymbol{\nabla})\tilde{\boldsymbol{u}} + \boldsymbol{\nabla}\boldsymbol{U}^{\mathrm{T}}\cdot\tilde{\boldsymbol{u}} - \boldsymbol{\nabla}\tilde{p} \end{pmatrix} \quad \text{and} \quad \mathscr{B}^\dagger(\tilde{p}, \tilde{\boldsymbol{u}}) = \begin{pmatrix} 0 \\ \tilde{\boldsymbol{u}} \end{pmatrix} \tag{3.7}$$

https://doi.org/10.1017/jfm.2013.90 Published online by Cambridge University Press

and associated with the boundary conditions

$$\partial_r \tilde{p}(x,0) = \partial_r \tilde{u}_x(x,0) = \tilde{u}_r(x,0) = 0 \quad \forall x \in [X_{in}, X_{out}] \tag{3.8a}$$

$$\tilde{\boldsymbol{u}}(X_{in}, r) = 0 \quad \forall r \in [0,1] \tag{3.8b}$$

$$\tilde{\boldsymbol{u}}(x,1) = 0 \quad \forall x \in [X_{in}, X_{out}] \tag{3.8c}$$

$$\boldsymbol{\sigma}^{\dagger}(\tilde{p}, \tilde{\boldsymbol{u}}) \cdot \boldsymbol{e}_x(X_{out}, r) = 0 \quad \forall r \in [0,1]. \tag{3.8d}$$

In addition, $\boldsymbol{\sigma}^{\dagger}$ is the adjoint stress tensor

$$\boldsymbol{\sigma}^{\dagger}(\tilde{p}, \tilde{\boldsymbol{u}}) = \frac{1}{Re}(\boldsymbol{\nabla}\tilde{\boldsymbol{u}} + \alpha_{out}\boldsymbol{\nabla}\tilde{\boldsymbol{u}}^{\mathrm{T}}) + (1-\beta_{out})\tilde{\boldsymbol{u}} \cdot \boldsymbol{U}^{\mathrm{T}} + \tilde{p}\boldsymbol{\delta}. \tag{3.9}$$

### 3.2. *Multi-domain discretization*

Among the various discretization methods employed in linear stability, the spectral collocation technique based on Chebychev interpolation is particularly well suited to regular solutions. Indeed, as explained by Canuto *et al.* (1988), if $u$ is a given function such as its $p$th derivative is continuous and $u_N$ its $N$-point Chebychev interpolation, then the error $u - u_N$ satisfies a relation that schematically reads as

$$\|u - u_N\|_{\Omega,w} \leqslant CN^{-p}\,\|u^{(p)}\|_{\Omega,w} \tag{3.10}$$

where $\|\ \|_{\Omega,w}$ is a quadratic norm on the domain $\Omega$ where $u$ is defined, pondered by a positive function $w$, typically $w(\xi) = \sqrt{1-\xi^2}$ when $\Omega = [-1,1]$. Yet the current stability problems are elliptic but non-normal: their solutions are actually regular, but they are expected to exhibit strong variations in thin zones near the domain boundaries, so that, even if the term $N^{-p}$ is small in the previous convergence relation, the norm of the $p$th-order derivative is large. Nevertheless, if a particular discretization is employed on such a thin zone, say $\Omega' \subset \Omega$, the relation (3.10) still holds with the pondered norm defined on $\Omega'$, so that $\|u^{(p)}\|_{\Omega',w'}$ is expected to be smaller and enhance the convergence.

In practice, the integration domain $\Omega = [X_{in}, X_{out}] \times [0,1]$ is divided into $P \times Q$ subdomains denoted as $D_{11}, \ldots D_{P1}, \ldots, D_{PQ}$, delimited by the axial and radial coordinates $x_0 = X_{in}, x_1, \ldots, x_{P-1}, x_P = X_{out}$ and $r_0 = 1, r_1, \ldots, r_{Q-1}, r_Q = 0$. On each domain $D_{pq}$ delimited by the points $(x_{p-1}, x_p)$ and $(r_{q-1}, r_q)$, a local double Gauss–Lobatto grid $(\xi_i, \eta_j)_{(i,j)\in[|1,N_p|]\times[|1,M_q|]}$ of size $(N_p, M_q)$ is set up and the Gauss–Lobatto variables are mapped to the physical variables $(x_i, r_j)$ by the variable changes $x_i = (x_p - x_{p-1})(1-\xi_i)/2 + x_{p-1}$ and $r_j = (r_q - r_{q-1})(1-\eta_j)/2 + r_{q-1}$. The spectral collocation technique allows us to express at any point $(x_k, r_l)$ the $n$th axial derivatives and $m$th radial derivatives of each variable $u$ as a linear combination of the elements $u(x_i, r_j)$, $(i,j) \in [|1, N_p|] \times [|1, M_q|]$ thanks to local derivation matrices denoted as $\boldsymbol{D}^{x,n}_{pq}$ and $\boldsymbol{D}^{r,m}_{pq}$. These are computed thanks to the algorithm introduced by Don & Solomonoff (1997), that is more accurate than the initial method presented by Canuto *et al.* (1988). Note that the above discretization ensures that the computed solutions are continuous; the continuity of the first axial and radial derivatives is imposed by adding interface conditions. To sum up, let $\boldsymbol{X}$ be a global vector containing the variables expressed at each point of the multi-domain bidimensional grid. The global discretized eigenvalue problem $\boldsymbol{AX} - \mathrm{i}\omega\boldsymbol{BX} = 0$ is assembled on each domain in two steps: first, the operators (3.3) or (3.7) are discretized thanks to the derivation matrices on the internal points; and, second, boundary conditions (3.4)–(3.8) or interface conditions are imposed on the points located at the boundaries.

https://doi.org/10.1017/jfm.2013.90 Published online by Cambridge University Press

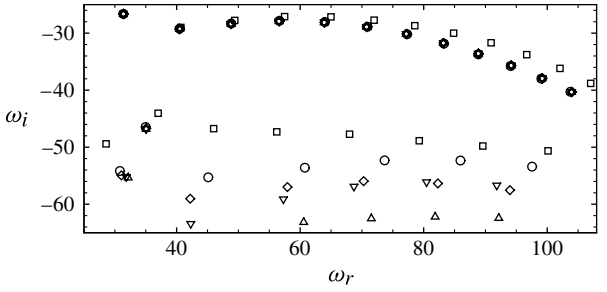



FIGURE 6. Spectra resulting from the global stability analysis of the Taylor–Culick flow, computed for $Re = 100$, $X_{in} = 4$ and $X_{out} = 8$. Direct eigenvalue problem solved with meshes $\text{MONO}_0$ (□), $\text{MULTI}_0^d$ (◇) and $\text{MULTI}_1^d$ (○), and adjoint problem solved with meshes $\text{MONO}_0$ (△) and $\text{MULTI}_0^a$ (▽).

| | $x_0$ | $N_1$ | $x_1$ | $N_2$ | $x_2$ | $N_3$ | $x_3$ |
|---|---|---|---|---|---|---|---|
| $\text{MONO}_0$ | 4 | 300 | 8 | | | | |
| $\text{MULTI}_0^d$ | 4 | 151 | 7.96 | 31 | 7.998 | 20 | 8 |
| $\text{MULTI}_1^d$ | 4 | 161 | 7.96 | 41 | 7.998 | 30 | 8 |
| $\text{MULTI}_0^a$ | 4 | 21 | 4.0004 | 31 | 4.04 | 150 | 8 |

TABLE 1. Axial discretization for the meshes used for global stability computations.

Finally, the resulting matrix eigenvalue problem is solved by the Krylov-subspace iteration technique of Arnoldi (1951), according to the methodology introduced by Rodríguez & Theophilis (2009). An eigenvalue target $\sigma$ with positive imaginary part is first chosen. Then, a cyclic-block decomposition of the matrix $\boldsymbol{A}_\sigma = \boldsymbol{A} - \mathrm{i}\omega\boldsymbol{B}$ is dispatched on a square grid of $n_{proc} \times n_{proc}$ processors and its lower–upper (LU) factorization is computed by calling the driver routines of the ScaLAPACK library (Blackford *et al.* 1997). Therefore, the Arnoldi algorithm allows a small set, say 20, of the largest eigenvalues of the matrix $\boldsymbol{A}_\sigma^{-1}\boldsymbol{B}$, in other words the closest eigenvalues to the target, and the related eigenvectors to be computed.

### 3.3. *Description of the eigenmodes*

In this section, we present the computed direct and adjoint stability modes, the analogies with the simplified previous convective–diffusive case, and the necessary mesh refinements carried out for growing Reynolds numbers. We first consider a computation performed for $Re = 100$ on the domain $[X_{in} = 4, X_{out} = 8]$. Three single-domain and multi-domain meshes, denoted as $\text{MONO}_0$ (for mono-domain), $\text{MULTI}_0^d$, $\text{MULTI}_1^d$ and $\text{MULTI}_0^a$ (for multi-domain), are used here. Their features are reported in table 1. The meshes $\text{MULTI}_0^d$ and $\text{MULTI}_0^a$ allow the respective outflow and inflow boundary layers of the direct and adjoint problems to be caught with more accuracy than with the initial mesh $\text{MONO}_0$. Here $\text{MULTI}_1^d$ is introduced to study the mesh convergence of the direct problem.

We first describe the spectra, computed by Arnoldi inverse iteration, presented in figure 6. The generated Krylov subspace is of size 200, so as to obtain 20 converged eigenvalues. Basically, two branches of discrete temporally damped modes are obtained. The upper one begins from the eigenvalue $\omega = 31.37 - 26.62\mathrm{i}$; its

https://doi.org/10.1017/jfm.2013.90 Published online by Cambridge University Press

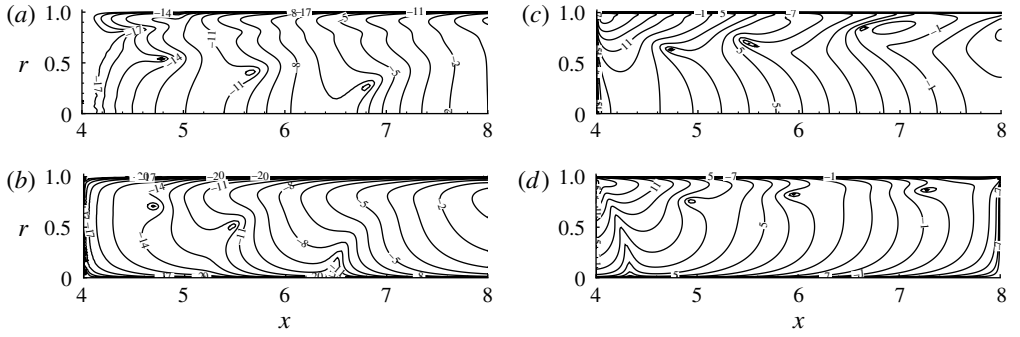



FIGURE 7. Isocontours of the eigenfunctions amplitude in logarithmic scale for the eigenmode $\omega = 56.55 - 27.91\mathrm{i}$, computed for $Re = 100$, $X_{in} = 4$ and $X_{out} = 8$. The direct axial ($a$) and radial ($b$) velocities are obtained with $\mathrm{MULTI}_0^d$; the adjoint axial ($c$) and radial ($d$) velocities are obtained with $\mathrm{MULTI}_0^a$. A normalization factor $1/u_x$ ($x = 7.5$, $r = 0.9$) is applied. Once again, the direct velocity fluctuations are amplified downstream and the adjoint ones decay away from $x = X_{in}$. One must note the existence of particular points where the amplitude tends towards zero, called 'amphidromic points'.

modes are of minimal temporal decay in the neighbourhood of the least stable one $\omega = 56.55 - 27.91\mathrm{i}$, and then are increasingly stable at higher frequency. Except for the mesh $\mathrm{MONO}_0$ that is too coarse, the modes neither depend on the used mesh nor the solved problem. Such a branch was previously obtained in the stability computations carried out on the whole cylinder by Chedevergne *et al.* (2006) and Chedevergne *et al.* (2012), but the location of each eigenvalue was strongly dependent on the axial discretization used. Therefore, the instabilities computed on a subdomain, in other words emerging from a parietal disturbance located at $X_{in}$, correspond to real eigenmodes of distinct frequencies rather than pseudo-modes. Note that it is not necessary to compute more modes on this branch because no instability corresponding to such $\omega_r$ has ever been measured experimentally, see Chedevergne *et al.* (2006). In the same way, the second branch, corresponding to even more stable modes, is not of great interest because their related instabilities would decay much more rapidly than those of the first branch. They are not as well converged as the latter ones, but a constant number of eigenvalues appears on a given range of reduced frequencies when the number of axial collocation points increases. For this reason, they may be actual modes rather than pseudo-modes as well. Conversely, as shown on the amplitude fields depicted in figure 7 for the mode $\omega = 56.55 - 27.91\mathrm{i}$, the temporally stable modes of the upper branch are related to spatially amplified direct eigenfunctions and decaying adjoint eigenfunctions. Both direct and adjoint velocity profiles reach their maximum amplitude in the vicinity of the blowing wall, for instance $r \approx 0.95$ for the direct axial fluctuations. The shape of the direct eigenfunctions are very similar to those obtained by Chedevergne *et al.* (2006) and those compared with the 'PVS' structures evidenced in cold-gas experiments by Griffond & Casalis (2001). As a consequence, these modes will be subsequently referred to as 'PVS instabilities'. Moreover, the logarithmic scale used in figure 7 allows us to quantify their growth. The constant step between each level denotes an exponential amplification, that is tentatively sought as $\hat{u}_x(x, r_0), \hat{u}_r(x, r_0) \approx a(r_0)x^{\lambda(r_0)}$ on each line of constant $r_0$. The typical polynomial growth of the eigenfunctions induced by uniformly accelerated base states, already observed in the above simplified modelling, is recovered here in spite of the domain

https://doi.org/10.1017/jfm.2013.90 Published online by Cambridge University Press

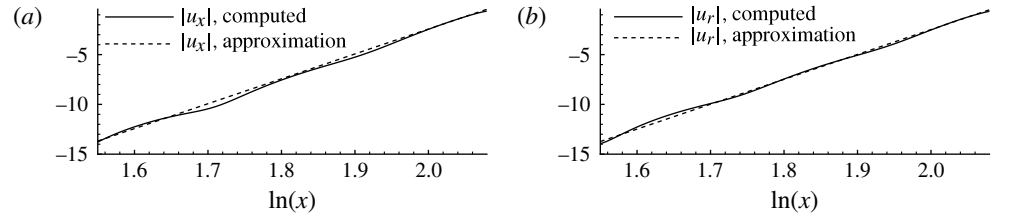



FIGURE 8. Axial ($a$) and radial ($b$) profiles of the logarithmic amplitude of the direct velocity fluctuations, and related approximations $\hat{u}_x(x, r_1) \approx a(r_1)x^{\lambda(r_1)}$ and $\hat{u}_r(x, r_2) \approx b(r_2)x^{\lambda(r_2)}$, with $r_1 = 0.91$, $r_2 = 0.66$, $\lambda(r_1) = \lambda(r_2) = 25$, as functions of $\log(x)$. The agreement is correct everywhere but in the neighbourhood of the outflow, where the imposed boundary condition induces a boundary layer in the same way as in the simplified convective–diffusive problem.

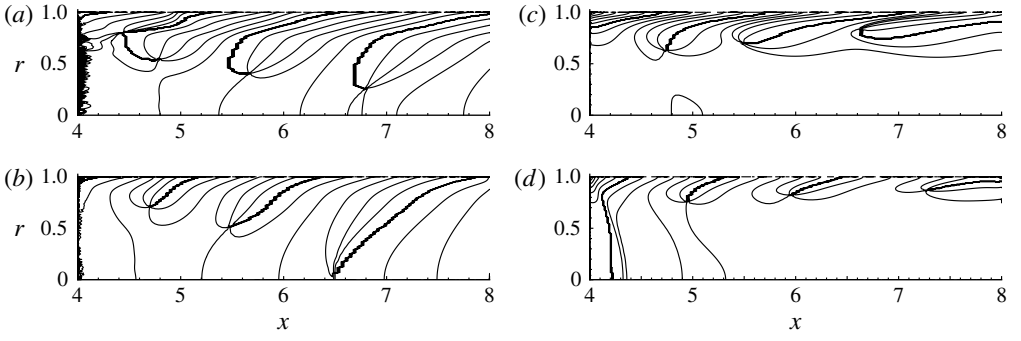



FIGURE 9. Phase isocontours of the eigenfunctions whose amplitude is presented in figure 7: ($a$) direct axial velocity; ($b$) direct radial velocity; ($c$) adjoint axial velocity; ($d$) adjoint radial velocity. The amphidromic points where the amplitude decays to zero correspond to the endpoints of the phase break lines here, so that the phase is not defined at these particular locations.

truncation. Note that the sought approximation does not take account of the inflow abscissa $X_{in}$. Provided that the selected lines of constant $r_0$ are far from particular points where the amplitude rapidly decays as highlighted in figure 7, a good agreement is found for both axial and radial direct velocity fluctuations with $\lambda(r_0) \approx 25$, see figure 8. The similarity with the eigenfunctions of the simplified stability problem also arises in the rough variations near the outflow boundary condition for the direct velocity fluctuations (figure 8).

In addition to the initial set of outflow boundary condition parameters, the choices $\alpha_{out} = 0$, $\beta_{out} = 0$ and $\alpha_{out} = 0$, $\beta_{out} = Re^{-1}$ have also been tested. The resulting eigenvalues are exactly similar to those depicted in figure 6. Correlatively, the eigenfunctions are only impacted at the outflow on a thin layer $x \in [(1 - \varepsilon)X_{out}, X_{out}]$ with $\varepsilon \approx 0.01$. This remarkable independence on the outflow parameters is very similar to that observed in the simplified problem (§ 2). This tends to prove that these eigenmodes basically depend on the imposed outflow pressure, but not on the viscous or convective terms included in the outflow boundary condition. In the further computations, $\alpha_{out}$ and $\beta_{out}$ will be set equal to zero.

Finally, special attention must be paid on the remarkable points where all of the velocity amplitudes presented in figure 7 decay down to zero. Correlatively, the phase fields depicted in figure 9 exhibit phase break lines that start from the wall

https://doi.org/10.1017/jfm.2013.90 Published online by Cambridge University Press

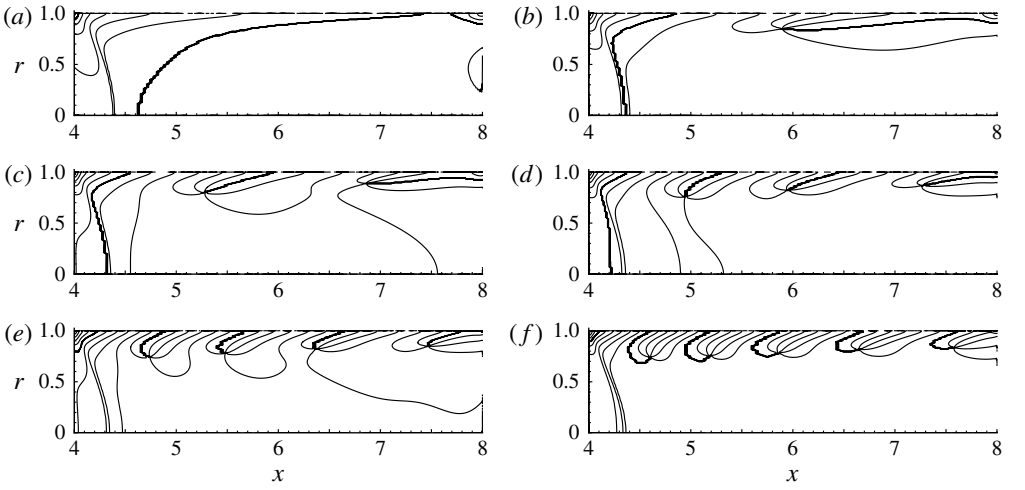



FIGURE 10. Phase isocontours of the adjoint radial velocity profile of the eigenmodes computed for $Re = 100$, $X_{in} = 4$ and $X_{out} = 8$ with MULTI$_0^a$: (*a*) mode $\omega = 31 - 27\mathrm{i}$; (*b*) $\omega = 40 - 29\mathrm{i}$; (*c*) $\omega = 49 - 28\mathrm{i}$; (*d*) $\omega = 57 - 28\mathrm{i}$; (*e*) $\omega = 63 - 28\mathrm{i}$; (*f*) $\omega = 71 - 29\mathrm{i}$.

and stop at these points, which means that the phase cannot be defined in these singular locations. Actually, the phase of the velocity fluctuations computed along time, namely $\mathrm{Re}(u'_x)/|u'_x|$ or $\mathrm{Re}(u'_r)/|u'_r|$, turns around these points, which are therefore called 'amphidromic points'. They separate two zones of the velocity fields: an upper area where a finite number of wavelengths occur along the axial coordinate; and a lower area where a single wavelength appears and all of the points are approximately in phase. Note also that the number of amphidromic points seems to define each mode of the upper branch: for instance, the radial adjoint velocity phase exhibits one more singularity for each subsequent mode of larger frequency, as presented for the first six eigenmodes in figure 10.

To conclude, actual discrete converged modes of the Taylor–Culick flow are exhibited in this section. Their direct and adjoint counterparts are computed correctly, and they are well identified by the number of amphidromic points occurring in the fields of velocity fluctuations that define a particular number oscillations in the axial direction. These general statements are of great interest with respect to the existence of modal instabilities in solid propellant motors.

### 3.4. *Influence of the viscosity and the domain extent*

Starting from the previous case $X_{in} = 4$, $X_{out} = 8$ and $Re = 100$, the influence of the inflow and outflow position and of the Reynolds number is studied. In this section, identical PVS branches of the spectra are obtained by solving the direct or adjoint stability equations. In figure 11, the sole adjoint spectra are exhibited. The employed meshes include again three axial partitions with boundaries that are the same as those of MULTI$_0^a$, but, if necessary, the number of points of the third partition is increased to reach mesh convergence. The Reynolds number has first been increased, stating from 100 up to 2000. As depicted in figure 11, a decreasing viscosity has a destabilizing effect on the eigenmodes, but the reduced frequencies are marginally impacted. In addition, the effect of such variations decreases at larger Reynolds numbers.

https://doi.org/10.1017/jfm.2013.90 Published online by Cambridge University Press

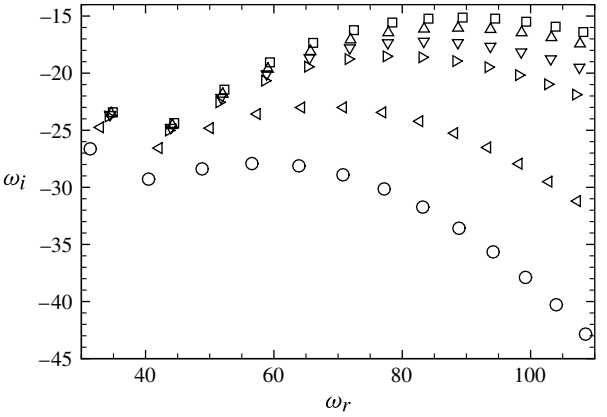



FIGURE 11. Spectra of the adjoint stability problem of the Taylor–Culick flow, computed for $X_{in} = 4$ and $X_{out} = 8$: (○) $Re = 100$; (◁) $Re = 200$; (▷) $Re = 500$; (▽) $Re = 700$; (△) $Re = 1000$; (□) $Re = 2000$.

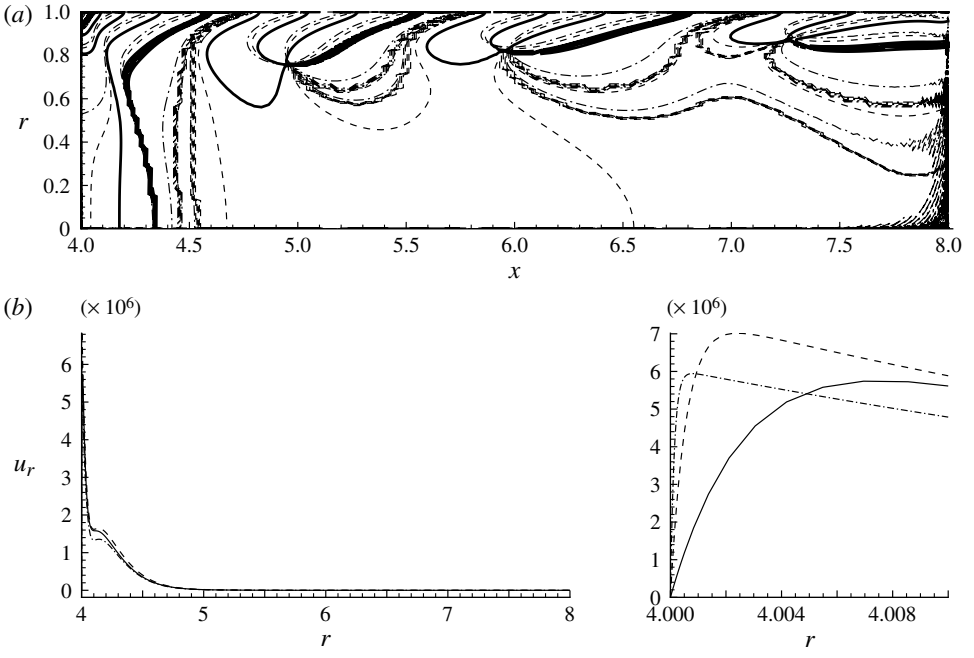



FIGURE 12. Adjoint radial velocity for the third eigenmode ($\hat{\omega}_r \approx 57$) computed for $Re = 100$ (solid lines), $Re = 500$ (dotted lines) and $Re = 2000$ (dashed lines); here $X_{in} = 4$ and $X_{out} = 8$. (*a*) Level lines of the phase field. (*b*) Global profiles at $r = 0.91$ (left) and zoom close to $x = X_{in}$ (right).

More remarkably, the location of the amphidromic points that define each mode is exactly the same for the three considered Reynolds numbers (see figure 12 for the phase fields). The only visible difference lies in the profile of the radial velocity near $x = X_{in}$: the upstream amplification of the eigenfunctions and the imposed inflow

https://doi.org/10.1017/jfm.2013.90 Published online by Cambridge University Press

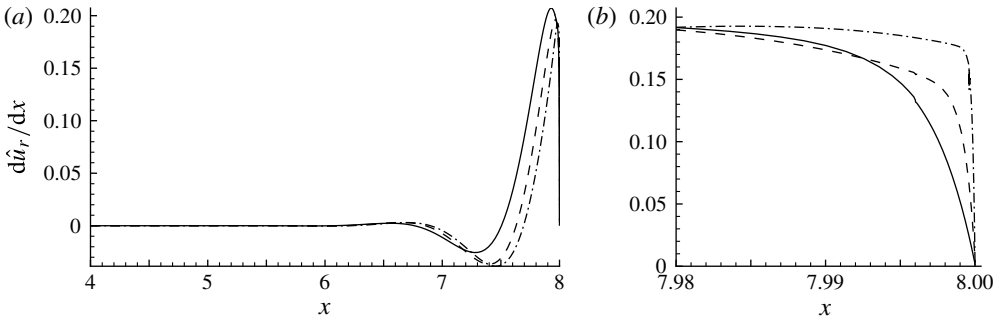



FIGURE 13. Direct radial velocity profiles for the third eigenmode ($\hat{\omega}_r \approx 57$) computed for $Re = 100$ (solid lines), $Re = 500$ (dotted lines) and $Re = 2000$ (dashed lines); here $X_{in} = 4$ and $X_{out} = 8$.

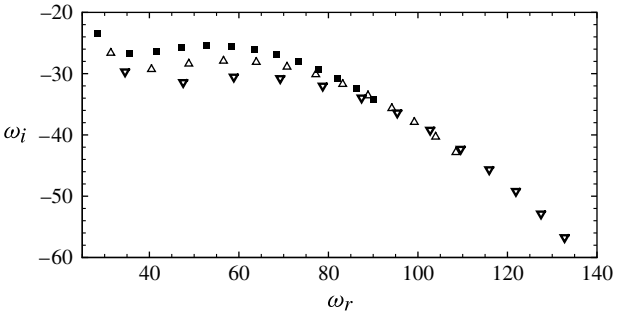



FIGURE 14. Spectra of the adjoint stability problem of the Taylor–Culick flow, computed for $Re = 100$ and $X_{out} = 8$: (■) $X_{in} = 3$; (△) $X_{in} = 4$; (▽) $X_{in} = 5$.

no-slip condition induces rough variations there which characteristic length is smaller for larger Reynolds numbers. The same observation holds for the axial derivative of the direct radial velocity profiles (figure 13), that are ended by a boundary layer at $x = X_{out}$. This typical feature already observed in the simplified stability problem is recovered here.

The variations of the inflow boundary location at constant output ($X_{out} = 8$) and Reynolds number ($Re = 100$) have then been investigated. The spectra plotted in figure 14 show that moving upstream the inflow switches the whole PVS branch towards the real axis. Conversely, for a fixed value of $X_{in}$, the eigenvalues remain approximately on the same branch and close up from each other when the duct length increases, as depicted in figure 15 where $X_{out}$ is increased from 7 to 9.5, still with $Re = 100$. In addition, the first mode of the branch ($\omega \approx 31 - 26\mathrm{i}$, no amphidromic point) clearly merges towards a fixed location, the second one ($\omega \approx 39 - 30\mathrm{i}$, one amphidromic point) is almost stabilized at $X_{out} = 9.5$, and the variations of the other eigenvalues becomes smaller at larger outflow abscissae. However, larger aspect ratios have not been tested since mesh convergence issues appear then. As in the simplified stability problem, the limit of the machine accuracy seems to be reached. In the next section, a sensibility analysis of these modes is carried out, and some critical elements of the numerical integration are exhibited.

https://doi.org/10.1017/jfm.2013.90 Published online by Cambridge University Press

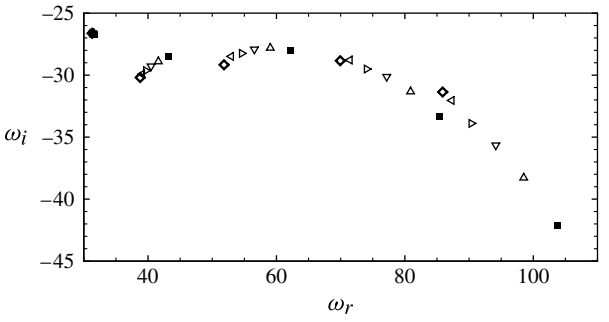



FIGURE 15. Spectra of the adjoint stability problem of the Taylor–Culick flow, computed for $Re = 100$ and $X_{in} = 4$: (■) $X_{out} = 7$; (△) $X_{out} = 7.5$; (▽) $X_{out} = 8$; (▷) $X_{out} = 8.5$; (◁) $X_{out} = 9$; (◇) $X_{out} = 9.5$. The modes with 0, 1, 3, 6 and 9 amphidromic points are represented.

## 4. Sensitivity analysis of the global stability problem

In this section, the effect of small disturbances on the global linearized Navier–Stokes operator is investigated. In the same way as for the simplified convective–diffusive problem, the shift $\varepsilon\delta\hat{\omega}$, due to perturbations on the boundary conditions or a small variation of the base data of amplitude $\varepsilon$, is obtained thanks to the Lagrange identity (3.6) that is linearized with respect to $\varepsilon$. In this respect, the counterpart of (2.11) reads

$$\delta\hat{\omega} = -\frac{\mathrm{i}}{(\tilde{\boldsymbol{u}}, \hat{\boldsymbol{u}})}\left[\int_{\partial\Omega} (\tilde{\boldsymbol{u}}^* \cdot \boldsymbol{\sigma}(\delta\hat{p}, \delta\hat{\boldsymbol{u}}) - \boldsymbol{\sigma}^{\dagger H}(\tilde{p}, \tilde{\boldsymbol{u}}) \cdot \delta\hat{\boldsymbol{u}})\mathrm{d}\sigma + \int_{\Omega} (\tilde{p}^*, \tilde{\boldsymbol{u}}^*; \delta\mathscr{A}(\hat{p}, \hat{\boldsymbol{u}}))\,\mathrm{d}\Omega\right], \tag{4.1}$$

where $(\delta\hat{p}, \delta\hat{\boldsymbol{u}})$ are the disturbances of the direct pressure and velocity fluctuations calculated at the boundaries, and $\delta\mathscr{A}$ a disturbance to the direct spatial operator. This expression will be derived to calculate the sensitivity function $\nabla_f\hat{\omega}$ of each parameter $f$, so that the contribution of $f$ to the eigenvalue variation is $\delta_f\hat{\omega} = \langle\nabla_f\hat{\omega}; f\rangle_E$, where $\langle\ ;\ \rangle_E$ denotes the hermitian dot product on the whole domain ($E = \Omega$) or on the boundary faces ($E$ is a subset of $\partial\Omega$, namely the inflow section $\Gamma_i$, the outflow section $\Gamma_o$ and the parietal boundary $\Gamma_p$).

### 4.1. *Sensitivity of the boundary conditions*

Expanding the first term of (4.1) allows to distinguish several sensitivity functions. At the wall and at the inflow cross-section, the direct velocity is imposed. Therefore, the eigenvalues are only sensible to errors $\delta\hat{\boldsymbol{u}}$ on the imposed velocity. More precisely, taking account for the adjoint boundary conditions, the following sensitivity functions are obtained:

$$\nabla^i_{\hat{u}_x}\hat{\omega} = \mathrm{i}\frac{\tilde{p}^*}{\langle\tilde{\boldsymbol{u}}, \hat{\boldsymbol{u}}\rangle}, \quad \nabla^i_{\hat{u}_r}\hat{\omega} = \mathrm{i}\frac{Re^{-1}\partial_x\tilde{u}^*_r}{\langle\tilde{\boldsymbol{u}}, \hat{\boldsymbol{u}}\rangle} \tag{4.2}$$

$$\nabla^p_{\hat{u}_x}\hat{\omega} = \mathrm{i}\frac{Re^{-1}\partial_r\tilde{u}^*_x}{\langle\tilde{\boldsymbol{u}}, \hat{\boldsymbol{u}}\rangle}, \quad \nabla^p_{\hat{u}_r}\hat{\omega} = \mathrm{i}\frac{\tilde{p}^*}{\langle\tilde{\boldsymbol{u}}, \hat{\boldsymbol{u}}\rangle}. \tag{4.3}$$

https://doi.org/10.1017/jfm.2013.90 Published online by Cambridge University Press

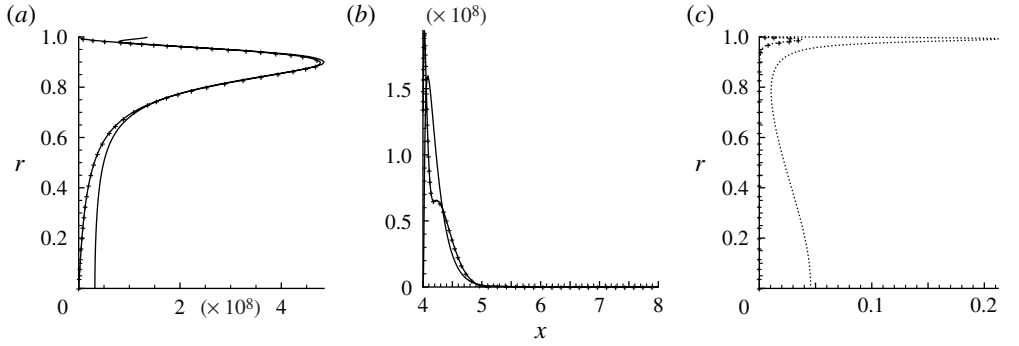



FIGURE 16. Amplitude of the sensitivity functions of the mode $\omega = 57 - 28\mathrm{i}$ obtained for $Re = 100$, $X_{in} = 4$ and $X_{out} = 8$: (*a*) inflow boundary condition; (*b*) wall boundary condition; (*c*) outflow boundary condition. Continuous lines: $\delta_{\hat{u}_x}\hat{\omega}$; continuous lines with symbols: $\delta_{\hat{u}_r}\hat{\omega}$; dashed lines: $\delta_{\partial_x\hat{u}_x}\hat{\omega}$; dashed lines with symbols: $\delta_{\partial_x\hat{u}_r}\hat{\omega}$. The sensitivity function related to the outflow pressure $\delta_{\hat{p}}\hat{\omega}$ is not shown in plot (*c*) since it is directly equal to $Re\delta_{\partial_x\hat{u}_x}\hat{\omega}$.

In contrast, the imposed outflow normal stress leads to gradients related to errors on the axial derivative of the velocity and on the pressure:

$$\nabla^o_{\partial_x\hat{u}_x}\hat{\omega} = \mathrm{i}\frac{Re^{-1}\tilde{u}^*_x}{\langle\tilde{\boldsymbol{u}},\hat{\boldsymbol{u}}\rangle}, \quad \nabla^o_{\partial_x\hat{u}_r}\hat{\omega} = \mathrm{i}\frac{Re^{-1}\tilde{u}^*_r}{\langle\tilde{\boldsymbol{u}},\hat{\boldsymbol{u}}\rangle} \quad \text{and} \quad \nabla^o_{\hat{p}}\hat{\omega} = -\mathrm{i}\frac{\tilde{u}^*_x}{\langle\tilde{\boldsymbol{u}},\hat{\boldsymbol{u}}\rangle}. \tag{4.4}$$

The results obtained are similar to those presented in § 2.2, insofar as the sensitivity functions are much larger for the inflow than for the outflow boundary condition (where they remain in $O(1)$) and rapidly decrease away from $x = X_{in}$ at the wall (figure 16). More precisely, the resulting sensitivity functions shall be compared with the machine accuracy $\varepsilon_M$ that may be employed as the linearization factor in the Lagrange identity to obtain the eigenvalue sensitivity (4.1). In this respect, a disturbance of order $\varepsilon_M$ (say $10^{-14}$) on the imposed axial derivative of the velocity fluctuations induces a shift on the eigenvalue that remains of order $\varepsilon_M$. In contrast, a disturbance of amplitude $\varepsilon_M$ applied to the velocity fluctuations at the wall close to $x = X_{in}$, or at the inflow boundary, may have the eigenvalue be displaced of about $\varepsilon_M\delta\hat{\omega} = 10^{-5}$ according to the plotted sensitivity functions. Such an uncertainty is large indeed, but not critical, in contrast to the simplified convection–diffusion problem, where the eigenvalue displacement $\varepsilon_M\delta\hat{\omega}$ could be as large as the eigenvalue itself.

### 4.2. *Sensitivity to a disturbance on the base state*

The present section aims at evaluating the sensitivity of the eigenvalues to small variations of the base state. This point is of great significance for physical purposes, since pressure oscillations are largely furthered by the existence of small geometric perturbations, e.g. a separation between two propellant grains, an emerging thermal protection or even irregularities on the propellant surface. These perturbations may induce slight modifications to the Taylor–Culick solution as steady state of the internal flow, whose influence can be quantified thanks to the above relation (4.1). More precisely, if a small disturbance $\delta\boldsymbol{U}$ is added to the base state, let $\delta\mathscr{A}(\hat{p},\hat{\boldsymbol{u}}) = (\delta\boldsymbol{U}\cdot\boldsymbol{\nabla})\hat{\boldsymbol{u}} + (\hat{\boldsymbol{u}}\cdot\boldsymbol{\nabla})\delta\boldsymbol{U}$ be the induced disturbance on the direct operator. Two sensitivity functions, related to the base flow velocity ($\nabla_{\boldsymbol{U}}\delta\hat{\omega}$) and its gradient ($\nabla_{\boldsymbol{\nabla U}}\delta\hat{\omega}$),

https://doi.org/10.1017/jfm.2013.90 Published online by Cambridge University Press

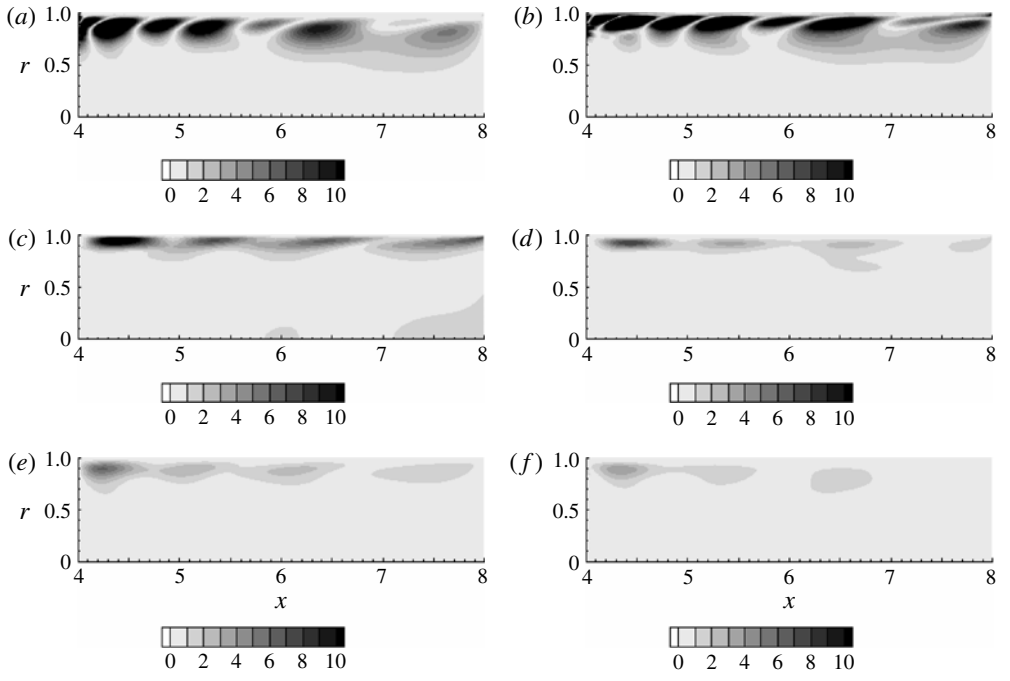



FIGURE 17. Amplitude of the sensitivity functions to base flow velocity modifications for the direct stability problem: (*a*) $\delta_{U_x}\hat{\omega}$; (*b*) $\delta_{U_r}\hat{\omega}$; (*c*) $\delta_{\partial_x U_x}\hat{\omega}$; (*d*) $\delta_{\partial_x U_r}\hat{\omega}$; (*e*) $\delta_{\partial_r U_x}\hat{\omega}$; (*f*) $\delta_{\partial_r U_r}\hat{\omega}$. Mode $\omega = 57 - 28\mathrm{i}$ obtained for $Re = 100$, $X_{in} = 4$ and $X_{out} = 8$.

respectively, are thus obtained:

$$\boldsymbol{\nabla}_{\boldsymbol{U}}\hat{\omega} = -\frac{\mathrm{i}\boldsymbol{\nabla}\hat{\boldsymbol{u}}^{\mathrm{T}}\tilde{\boldsymbol{u}}^{*}}{\langle\tilde{\boldsymbol{u}},\hat{\boldsymbol{u}}\rangle} \quad \text{and} \quad \boldsymbol{\nabla}_{\boldsymbol{\nabla U}}\hat{\omega} = -\frac{\mathrm{i}\tilde{\boldsymbol{u}}^{*}\otimes\hat{\boldsymbol{u}}}{\langle\tilde{\boldsymbol{u}},\hat{\boldsymbol{u}}\rangle}. \tag{4.5}$$

These sensitivities shall be associated with the non-normality rooted in the convective terms of the linearized incompressible Navier–Stokes equations. The global non-normality is quantified by the ratio $\zeta = \|\tilde{\boldsymbol{u}}\|\|\hat{\boldsymbol{u}}\|/(\tilde{\boldsymbol{u}},\hat{\boldsymbol{u}})$, necessarily larger than one. Then, in contrast to the simplified stability problem of § 2, two sources of non-normality can be identified (Marquet *et al.* 2009). The first is related to the convection of the velocity fluctuations by the base state, and implies that the direct and adjoint eigenfunctions are amplified in opposite directions. The second causes the direct and adjoint eigenfunctions to reach their maximum amplitude in a different velocity component, and is associated with the transposition of the base flow velocity gradient between the direct and the adjoint problems. It is quantified by the ratio $\eta = \langle\|\tilde{\boldsymbol{u}}\|,\|\hat{\boldsymbol{u}}\|\rangle/\|\tilde{\boldsymbol{u}}\|\|\hat{\boldsymbol{u}}\|$, where $\langle\ ,\ \rangle$ denotes here the dot product between two scalar fields defined on the domain $\Omega$. Therefore, splitting up $\zeta$ as $\zeta = \eta\zeta + (1-\eta)\zeta$ allows us to quantify the respective effect of each source of non-normality. In addition, one obtains easily that $\eta\zeta = \|\boldsymbol{\nabla}_{\boldsymbol{\nabla U}}\hat{\omega}\|$: in other words, the component-type non-normality can be quantified by considering the sensitivity to modifications on the velocity gradient.

Once again, the mode $\omega = 57 - 28\mathrm{i}$ obtained with parameters $Re = 100$, $X_{in} = 4$ and $X_{out} = 8$ is analysed. As depicted in figure 17, the higher base flow sensitivity zones are located in a thin band close to the wall, and rather upstream. This indicates that

https://doi.org/10.1017/jfm.2013.90 Published online by Cambridge University Press

small disturbances on the main velocity field, such as those usually caused by thermal protections or intersegments in real configurations, may have a severe influence on the eigenmodes if they occur in the head end zone; in contrast, if the base flow slightly differs from the Taylor–Culick solution, which is physically relevant in longer cylinders ($X_{out} > 12$) with partly turbulent zones (Varapaev & Yagodkin 1969; Brown *et al.* 1981; Avalon & Josset 2006), then the eigenvalues are not expected to be noticeably impacted upon. In addition, the sensitivity functions related to the sole base flow convection $\boldsymbol{U}$ are markedly larger than the other ones. The non-normality is thus dominated by the convective effects, which may be verified in the shape of the eigenfunctions depicted in figure 7: the counterpart of the large downstream growth of the direct velocity fluctuations is the even larger upstream amplification of the adjoint ones, whereas both axial and radial components are of equal amplitude. This convective sensibility can be further analysed by evaluating an optimal base flow disturbance that maximizes the perturbation on the eigenvalues. The method introduced by Bottaro *et al.* (2003) can be easily carried out thanks to the assumption of infinitesimal disturbances. In that case, the optimal velocity perturbation $\delta U_x$ (or $\delta U_r$) is colinear to the sensitivity function $\nabla_{U_x}\hat{\omega}$ (or $\nabla_{U_r}\hat{\omega}$) and the modulus of the eigenvalue variation is directly $|\delta\hat{\omega}| = \|\nabla_{U_x}\hat{\omega}\|\|\delta U_x\|$ (or $|\delta\hat{\omega}| = \|\nabla_{U_r}\hat{\omega}\|\|\delta U_r\|$). For the eigenmode $\omega = 57 - 28\mathrm{i}$, the resulting norm of the optimal sensitivities are $\|\boldsymbol{\nabla}_{U_x}\hat{\omega}\| \approx 10$ and $\|\boldsymbol{\nabla}_{U_r}\hat{\omega}\| \approx 15$ for the optimal axial and radial base flow disturbances. These values remain lower than 175 for all of the considered eigenmodes of the cases $(Re = 100, X_{in} = 4, X_{out} = 8)$, $(Re = 500, X_{in} = 4, X_{out} = 8)$ and are even lower for the case $(Re = 100, X_{in} = 4, X_{out} = 7)$. Therefore, these values ensure that the direct stability problem is robust to numerical errors or small uncertainties on the base flow if the their norm is smaller than, say, $10^{-3}$, so that $\delta\hat{\omega}$ remains much smaller than 1. However, considering the limit of linear base flow disturbances ($\|\delta U_x\|/\|U_x\| \approx 0.1$ or $\|\delta U_r\|/\|U_r\| \approx 0.1$, with $\|U_x\| \approx 19.8$ and $\|U_r\| \approx 1.3$), the above optimal disturbances can lead to eigenvalues modifications much larger than 1. Therefore, the effect of a wall defect imposed at a maximum peak of sensitivity field may completely change the shape of the spectrum.

## 5. Final discussion

In this work, the possible existence of separated instability modes of the internal flows of SRMs, modelled as cylindrical ducts with blowing walls, has been investigated. The modes computed in purely smooth configurations, that have been shown to have a physical relevance but also a strong dependence on the axial discretization in previous works (Chedevergne *et al.* 2012), can now be re-interpreted as pseudo-modes that verify the stability equations up to a small error. Indeed, the analytical study of a simplified monodimensional convective–diffusive stability problem whose convective term, as the Taylor–Culick flow, is proportional to the axial coordinate, provides helpful hints on the numerical criticality of the global stability of SRMs. This numerical stiffness arises as follows: first, the axial polynomial amplification of the eigenfunctions, mostly related to the accelerated base state, induces a ratio between the inflow and the outflow amplitudes that reaches the machine accuracy; second, a continuous set of pseudo-modes up to the machine accuracy can be exhibited when the Reynolds number is larger than a critical value; third, the boundary condition at $x = 0$ shows a dramatic sensitivity to numerical disturbances. Since the global problem presents the same features, it can be assumed

https://doi.org/10.1017/jfm.2013.90 Published online by Cambridge University Press

that the global modes computed from the head end are pseudo-modes, and that hydrodynamic instabilities hardly emerge at discrete frequencies in these conditions.

That is why the effect of a wall defect occurring at a given position $X_{in}$, where the PVS structures have been shown to emerge (Boyer *et al.* 2012), has been explicitly taken into consideration in the present global stability analysis by assuming that the resulting modes only propagate between $X_{in}$ and the outflow boundary located at $X_{out}$. Among the resulting eigenmodes, the most unstable branch is of particular interest. Its eigenvalues do not depend on further mesh refinements if the boundary layer zones are computed correctly; the related fields of velocity fluctuations exhibit a finite number of nodal or amphidromic points, and one point is added to each mode of larger circular frequency. In contrast to the simplified problem, the inflow sensitivity is not critical insofar as it cannot switch the eigenvalues to different locations in the complex plane.

These results thus indicate that the current modal approach, although difficult from a numerical standpoint, can be used to model the instabilities of the Taylor–Culick flow that emerge from a spatial disturbance. In this framework, a parametric study indicates a marginal influence of an increasing Reynolds number, in particular on the frequencies and the location of the amphidromic points. In contrast, the whole branch of eigenmodes is temporally stabilized when the inflow boundary condition is switched downstream, whereas the eigenvalues close up to each other on the same branch when the duct length is increased, the inflow being fixed. The sensitivity analysis of the eigenvalues to base flow modifications has been also evaluated. The sensitivity functions basically show larger amplitudes close to the inflow boundary and the blowing wall; they exhibit then several local peaks whose amplitudes decrease along $x$. This shows that the eigenmodes may be largely modified by adding slight parietal disturbances located upstream. In contrast, the effect of perturbations is much smaller downstream, so that the effect of the usual disturbances due to turbulent transition that occur at large $x$ might be negligible. Anyway, the optimal base flow perturbations remain bounded for all of the eigenmodes: the existence of discrete eigenvalues is therefore robust to small modifications on the base state.

To conclude with, the present paper shows the relevance of the enhanced modal approach introduced by Boyer *et al.* (2012) to perform the stability analysis of the internal flow of SRMs. In contrast to the analysis previously carried out on the whole domain (Chedevergne *et al.* 2006, 2012), the resulting discrete modes show similar features as those computed in boundary layer stability (Ehrenstein & Gallaire 2005; Alizard & Robinet 2007; Åkervik *et al.* 2008), even if they are still much more amplified in the axial direction. In this respect, further questions may be raised about the Taylor–Culick flow dynamics. Indeed, such temporally stable modes, although discrete, are supposed to carry physical information collectively but not individually in the case of noise amplifiers corresponding to convectively unstable modes (Sipp *et al.* 2010). For instance, the convection of a wave packet modelled as a large superimposition of eigenmodes has been evidenced in the works of Ehrenstein & Gallaire (2005). In the case of SRM, the physical relevance of each mode shall be further investigated. In particular, the eigenmodes computed here shall be compared with instabilities actually measured experimentally or computed by numerical simulation. Then, the mechanisms leading to the well-known appearance of pressure oscillations of discrete frequencies may be interpreted in the light of the notions of forced response, since the PVS is excited by external sources, and transient growth that typically play a major role in convectively unstable flows.

https://doi.org/10.1017/jfm.2013.90 Published online by Cambridge University Press

**Acknowledgements**

This study has been performed with the financial support of the French Centre National d'Études Spatiales (CNES) and the participation of the ONERA. The authors would like to thank in particular N. Cesco, Ph. Supie and E. Robert (CNES), M. Prevost (ONERA Fauga) and G. Avalon (ONERA Palaiseau) for their technical assistance. They are also very grateful to Ph. Villedieu (ONERA Toulouse) for fruitful discussions.

## Appendix. Theoretical details on the convective–diffusive simplified case

### A.1. *External development*

The solution of the eigenvalue problem (2.1) is sought as an asymptotic expansion $U_N(x) = u_0(x) + Re^{-1}u_1(x) + \cdots + Re^{-N}u_N(x)$ with respect to the small parameter $Re^{-1}$ on a subdomain $[0, a]$ where $a$ is arbitrarily close to 1. Here $U_N$ is thus assumed to take the inflow boundary condition $U_N(0) = 0$, but no condition is imposed at $x = a$. In the above development, the functions $u_n$ are assumed to remain bounded on the whole domain, i.e. $u_n = O(1)$. Therefore, $(\mathscr{A} - \mathrm{i}\hat{\omega})U_N$ can be re-expressed into separate terms related to the growing powers of $Re^{-1}$. If each order is set equal to zero, then the recursive system of ordinary differential equations with initial conditions

$$xu_0' - \mathrm{i}\hat{\omega}u_0 = 0; \quad u_0(0) = 0 \tag{A 1}$$

$$xu_n' - \mathrm{i}\hat{\omega}u_n = u_{n-1}''; \quad u_n(0) = 0 \quad \forall n = 1, \ldots, N \tag{A 2}$$

is obtained. The following generic term is calculated by recursive integration:

$$u_n(x) = \frac{c_n(\hat{\omega})}{n!\,(-2^2)^n} x^{\mathrm{i}(\hat{\omega}-2n)}, \tag{A 3}$$

where $c_0(\hat{\omega}) = 1$, $c_n(\hat{\omega}) = (\mathrm{i}\hat{\omega})(\mathrm{i}\hat{\omega} - 1)\ldots(\mathrm{i}\hat{\omega} - 2n + 1)$ for $n = 1, \ldots, N$. In addition, $U_N$ exactly verifies (2.1) if the residual

$$r_N(\hat{\omega}) = ((\mathscr{A} - \mathrm{i}\hat{\omega})U_N)(x) = \frac{c_{N+1}(\hat{\omega})}{Re^{N+1}N!\,(-2)^N} x^{\mathrm{i}\hat{\omega}-2N} \tag{A 4}$$

is nullified, which implies that $\mathrm{i}\hat{\omega} \in \{1, 2, \ldots, 2n - 1\}$. Among these values of $\mathrm{i}\hat{\omega}$, only the odd ones allow the initial condition $U_N(0) = 0$ to be satisfied. As a conclusion, $N$ eigenpairs are obtained by calculating the above $N$th-order expansion. For the $m$th solution that corresponds to the eigenvalue $\hat{\omega}_m = -(2m - 1)\mathrm{i}$ with $m = 1, \ldots, N$, the coefficients $c_n$ cancel for $n > m$ and the expansion is reduced to a sum of $m$ terms. The eigenpairs eventually read

$$\left\{ \hat{\omega}_m = -(2m + 1)\mathrm{i},\ U_m(x) = \sum_{n=0}^{m} \frac{(2m + 1)!}{(2(m - n) + 1)!n!\,(-2Re)^n} x^{2(m-n)+1} \right\}_{m=0,\ldots,N}. \tag{A 5}$$

### A.2. *Internal development and matching conditions*

The above eigenfunctions do not account for the outflow boundary condition. Therefore, the variable change $\hat{v}(X = Re(1 - x)) = \hat{u}(x)$ is introduced so as to calculate the particular shape of the eigenfunctions in the neighbourhood of $x = 1$. The eigenvalue problem is thus re-expressed as

$$(\hat{v}'' + \hat{v}') - \frac{1}{Re}(\hat{v}' - \mathrm{i}\hat{\omega}\hat{v}) = 0. \tag{A 6}$$

https://doi.org/10.1017/jfm.2013.90 Published online by Cambridge University Press

As earlier, $\hat{v}$ is approximated as a $K$th-order asymptotic expansion $\hat{v}(X) \approx U_K(X) = v_0(X) + Re^{-1}v_1(X) + \cdots + Re^{-K}v_K(X)$, where $K$ is not necessarily equal to $N$ and $v_k = O(1)$ for all $k$. Introducing this expression in (A 6) leads to the recursive system

$$v_0'' + v_0' = 0 \tag{A 7}$$

$$v_{k+1}'' + v_{k+1}' = Xv_k' - \mathrm{i}\omega v_k \quad \forall k = 1, \ldots, K. \tag{A 8}$$

The recursive integration of each generic term $v_k$ shows that

$$v_k(X) = P_k(X) + Q_k(X)\mathrm{e}^{-X} \tag{A 9}$$

where $P_k$ and $Q_k$ are polynomial functions of degree $k$ and $2k-2$, respectively, verifying the recurrence relations

$$P_{k+1}'' + P_{k+1}' = XP_k' - \mathrm{i}\hat{\omega}P_k \tag{A 10}$$

$$Q_{k+1}'' - Q_{k+1}' = X(Q_k' - Q_k) - \mathrm{i}\hat{\omega}Q_k. \tag{A 11}$$

Moreover, the boundary condition $V_K'(0) = 0$ implies that

$$P_k'(0) + Q_k'(0) - Q_k(0) = 0. \tag{A 12}$$

Therefore, the global solution can be expressed as a sum of two independent solutions $V_K(X) = V_{K,1}(X) + V_{K,2}(X)$ such as

$$V_{K,1}(X) = \sum_{k=0}^{K} Re^{-k}P_k(X) \quad \text{and} \quad V_{K,2}(X) = \left(\sum_{k=0}^{K} Q_k(X)\right)\mathrm{e}^{-X}. \tag{A 13}$$

On the one hand, if the set of polynomials $P_k$ is of size $K = 2m+1$, then $V_{K,1}(X)$ can be identified with the external part of the $m$th eigenfunction $\hat{u}_m$ of the set (A 5), expressed as $\hat{v}_m(X) = \hat{u}_m(x = 1 - X/Re)$. Indeed, $V_{K,1}$ does not depend on the outflow condition since the $P_k$ polynomials appear with a first-order derivative in (A 12); it satisfies the same differential equation as $\hat{u}_m$ apart from the variable change $X = Re(1-x)$ and admits the same polynomial form. On the other hand, $V_{K,2}(X)$ is exponentially small as soon as $X \gg 1$, i.e. when $1 - x \gg 1/Re$, so that the global solution is hardly disturbed in the external zone, but fits to the imposed boundary condition at $x = 1$ and behaves like a boundary layer.

Practically, $P_k$ and $Q_k$ may be written as

$$P_k(X) = \sum_{p=0}^{K} a_{kp}X^p \quad \text{and} \quad Q_k(X) = \sum_{p=0}^{2K-2} b_{kp}X^p. \tag{A 14}$$

The $a_{kp}$ are directly obtained by the identification with the coefficients of the external solution. Then, the $b_{kp}$ are obtained by the recurrence relation (A 11) for $p \geqslant 1$, and by the expression of the outflow condition (A 12) for $p = 0$ that reads $a_{k1} + b_{k1} - b_{k0} = 0$. In particular, for the two first eigenmodes $\hat{\omega}_0 = -\mathrm{i}$ and $\hat{\omega}_1 = -3\mathrm{i}$, one obtains the following re-expressed external solutions:

$$\hat{v}_0(X) = \hat{u}_0(x = 1 - Re^{-1}X) = 1 - Re^{-1}X \tag{A 15a}$$

$$\hat{v}_1(X) = \hat{u}_1(x = 1 - Re^{-1}X) = 1 - 3Re^{-1}X + 3Re^{-2}X^2 - Re^{-3}X^3. \tag{A 15b}$$

This induces the following $Q_k$ polynomials:

$$Q_0 = 0 \quad \text{and} \quad Q_1 = -1 \quad \text{for } \hat{u}_0 \tag{A 16}$$

https://doi.org/10.1017/jfm.2013.90 Published online by Cambridge University Press

and

$$Q_0 = 0, \tag{A 17a}$$

$$Q_1 = -3 \tag{A 17b}$$

$$Q_2 = -(3X^2/2 + 12X + 9) \tag{A 17c}$$

and

$$Q_3 = -(3X^4/8 + 15X^3/2 + 111X^2/2 + 139X + 139) \quad \text{for } \hat{u}_1. \tag{A 17d}$$

Therefore, the total eigenfunctions including the viscous outflow correction read

$$\hat{u}_0(x) = x - \frac{\mathrm{e}^{Re(x-1)}}{Re} \tag{A 18}$$

$$\hat{u}_1(x) = x^3 - \frac{3x}{Re} - \left( \frac{3Re\,(1-x)^4}{8} + \frac{15\,(1-x)^3 + 3\,(1-x)^2}{2} + \frac{(111\,(1-x)^2 + 24(1-x) + 6)}{2Re} + \frac{(139(1-x)+9)}{Re^2} + \frac{139}{Re^3} \right) \mathrm{e}^{Re(x-1)}. \tag{A 19}$$

As a conclusion, eigenfunctions approximated as a full matched asymptotic expansion can be decomposed into a first part that only depends on the inflow boundary condition and the order of its related eigenvalue, and a second part that is merely a correction added to capture the outflow boundary condition, but that has no influence on the eigenvalues.

## REFERENCES


AIRIAU, C. 2000 Non-parallel acoustic receptivity of a Blasius boundary layer using an adjoint approach. *Flow Turbul. Combust.* **65** (3/4), 347–367.

ÅKERVIK, E., EHRENSTEIN, U., GALLAIRE, F. & HENNINGSON, D. S. 2008 Global two-dimensional stability measures of flate plate boundary layer flow. *Eur. J. Mech. (*B/*Fluids*) **27**, 501–513.

ALIZARD, F. & ROBINET, J.-C. 2007 Spatially convective global modes in a boundary layer. *Phys. Fluids* **19**.

ARNOLDI, W. E. 1951 The principle of minimized iteration in the solution of the matrix eigenvalue problem. *Q. Appl. Maths* **9**, 17–29.

AVALON, G. & JOSSET, T. 2006 Cold gas experiments applied to the understanding of aeroacoustic phenomena inside solid propellant rockets. In *42nd AIAA/ASME/SAE/ASEE Joint Propulsion Conference and exhibit, Sacramento, California*.

BLACKFORD, L. S., CHOI, J., CLEARY, A., D'AZEVEDO, E., DEMMEL, J., DHILLON, I., DONGARRA, J., HAMMARLING, S., HENRY, G., PETITET, A., STANLEY, K., WALKER, D. & WHALEYY, R. C. 1997 Scalapack: a linear algebra library for message-passing computers.

BOTTARO, A., CORBETT, P. & LUCCHINI, P. 2003 The effect of base flow variation on flow stability. *J. Fluid Mech.* **476**, 293–302.

BOYER, G., CASALIS, G. & ESTIVALÈZES, J.-L. 2012 Theoretical investigation of the parietal vortex shedding in solid rocket motors. In *48th AIAA/ASME/SAE/ASEE Joint Propulsion Conference and Exhibit, Atlanta, Georgia*.

BRANDT, L., SIPP, D., PRALITS, J. O. & MARQUET, O. 2011 Effects of base-flow variation in noise amplifiers: the flat-plate boundary layer. *J. Fluid Mech.* **687**, 503–528.

BROWN, R. S., DUNLAP, R., YOUNG, S. W. & WAUGH, R. C. 1981 Vortex shedding as a source of acoustic energy in segmeted solid motor rockets. *J. Spacecraft* **18**, 312–319.

CANUTO, C., HUSSAINI, Y. M., QUARTERONI, A. & ZANG, T. A. 1988 *Spectral Methods in Fluid Dynamics*. Springer.

CASALIS, G., AVALON, G. & PINEAU, J. PH. 1998 Spatial instability of planar channel flow with fluid injection through porous walls. *Phys. Fluids* **10**, 2258–2568.

CHEDEVERGNE, F. 2007 Instabilités intrinsèques des moteurs à propulsion solide. PhD thesis, ENSAE.


https://doi.org/10.1017/jfm.2013.90 Published online by Cambridge University Press

CHEDEVERGNE, F., CASALIS, G. & FERAILLE, T. 2006 Biglobal linear stability analysis of the flow induced by wall injection. *Phys. Fluids* **18**.

CHEDEVERGNE, F., CASALIS, G. & MAJDALANI, J. 2012 Direct numerical simulation and biglobal stability investigations of the gaseous motion in solid rocket motors. *J. Fluid Mech.* **706**, 190–218.

CULICK, F. 1966 Rotational axisymmetric mean flow and damping of acoustic waves in a solid propellant rocket. *AIAA J.* **4**, 1462–1464.

DON, W. S. & SOLOMONOFF, A. 1997 Accuracy enhancement for higher derivatives using Chebyshev collocation and a mapping technique. *SIAM J. Sci. Comput.* **18** (4), 1040–1055.

DUNLAP, R., BLACKNER, A. M., WAUGH, R. C., BROWN, R. S. & WILLOUGHBY, P. G. 1990 Internal flow field studies in a simulated cylindrical port rocket chamber. *J. Propulsion* **6** (6), 290–704.

EHRENSTEIN, U. & GALLAIRE, F. 2005 On two-dimensional temporal modes in spatially evolving open flows: the flat-plate boundary layer. *J. Fluid Mech.* **536**, 209–218.

FLANDRO, G. A. 1995 Effects of vorticity on rocket combustion stability. *J. Propul. Power* **11** (4), 607–625.

FLANDRO, G. A. & MAJDALANI, J. 2003 Aeroacoustic instability in rockets. *AIAA J.* **41**, 485–497.

GRIFFOND, J. & CASALIS, G. 2001 On the nonparallel stability of the injection induced two-dimensional Taylor flow. *Phys. Fluids* **13** (1635).

HILL, D. C. 1995 Adjoint systems and their role in the receptivity problems for boundary layers. *J. Fluid Mech.* **292**, 183–204.

MAJDALANI, J. 2009 Multiple asymptotic solutions for axially travelling waves in porous channels. *J. Fluid Mech.* **636** (1), 59–89.

MAJDALANI, J., FISCHBACH, S. R. & FLANDRO, G. A. 2006 Improved energy normalization function in rocket motor stability calculations. *Aerosp. Sci. Technol.* **10**, 495–500.

MARQUET, O., LOMBARDI, M., CHOMAZ, J.-M., SIPP, D. & JACQUIN, L. 2009 Direct and adjont global modes of a recirculation bubble: lift-up and convective non-normalities. *J. Fluid Mech.* **622**.

MARQUET, O., SIPP, D. & JACQIN, L. 2008 Sensitivity analysis and passive control of cylinder flow. *J. Fluid Mech.* **615**, 221–252.

MONOKROUSOUS, A., ÅKERVIK, E., BRANDT, L. & HENNINGSON, D. S. 2010 Global three-dimensional optimal disturbances in the Blasius boundary layer flow using time-steepers. *J. Fluid Mech.* **650**.

PRÉVOST, M. & GODON, J.-C. 2005 Thrust oscillations in reduced scale solid rocket motors. Part 1. Experimental investigations. In *41nd AIAA/ASME/SAE/ASEE Joint Propulsion Conference and exhibit, Tucson, Arizona*.

RODRÍGUEZ, D. & THEOPHILIS, V. 2009 Massively parallel solution of the BiGlobal eigenvalue problem using dense linear algebra. *AIAA J.* **47**, 2449–2459.

SIPP, D., MARQUET, O. & MEGLIA, PH. 2010 Dynamics and control of global instabilities in open flows; a linearized approach. *Appl. Mech. Rev.* **63**.

TAYLOR, G. I. 1956 Fluid flows in regions bounded by porous surfaces. *Proc. R. Soc. Lond., Ser. A, Math. Phys. Eng. Sci.* **234** (1199), 456–475.

THEOFILIS, V. 2003 Advances in global linear instability analysis of nonparallel and three-dimensional flows. *Prog. Aerosp. Sci.* **39**, 249–315.

TREFETHEN, L.-N. & EMBREE, M. 2005 *Spectra and Peudospectra*. Princeton University Press.

TREFETHEN, L. N., TREFETHEN, A. E., REDDY, S. C. & DRISCOLL, T. A. 1993 Hydrodynamic stability without eigenvalues. *Science* **261**.

TUMIN, A. 2003 Multimode decomposition of spatially growing perturbations in a two-dimensional boundary layer. *Phys. Fluids* **15** (9), 2525–2540.

VARAPAEV, V. N. & YAGODKIN, V. I. 1969 Flow instability in a channel with porous wall. *Izv. Acad. Nauk SSSR Mekh. Zhidk. Gaza* **4** (5).

VUILLOT, F. 1995 Vortex shedding phenomena in solid propellant motors. *J. Propul. Power* **11** (4), 626–639.

YAGODKIN, V. I. 1967 Use of channels with porous walls for studying flows which occur during combustion of solid propellants. In *18th International Astronautical Congress AGARD*.

https://doi.org/10.1017/jfm.2013.90 Published online by Cambridge University Press